Effects of rupture source and fringing reefs on the 2009 South Pacific tsunami inundation on southeast Upolu Island, Samoa

Cyprien Bosserelle[1,1], Shaun Williams[1,1], Kwok Fai Cheung[2,2], Titimanu Simi[3,3], Yoshiki Yamazaki[2,2], Volker Roeber[4,4], Thorne Lay[5,5], Emily M. Lane[6,6], Ryan Paulik[1,1], and Lameko Simanu[7,7]

[1]National Institute of Water and Atmospheric Research
[2]University of Hawaii at Manoa
[3]Ministry of Finance
[4]Univ Pau & Pays Adour
[5]University of California Santa Cruz
[6]National Institute for Water and Atmospheric Research
[7]Ministry of Natural Resources and Environment

November 30, 2022

Abstract

The subduction zone along the northern Tonga Trench has the highest plate convergence rate in the world, but limited records of its seismic and tsunamigenic activities. In 2009, a tsunami generated by an MW 8.1 earthquake doublet caused severe impacts in the region including damage and loss of life on the south shores of Upolu and Savaii Islands, Samoa. Here we use numerical modeling aided by recorded data and eyewitness accounts to evaluate which of the published source models in the Tonga Trench region most suitably represents the 2009 event for use in hazard assessment around Samoa. We show that only a few of the published sources are suitable to reproduce large inundation observed in Samoa and none reproduces runup as high as observed in areas that were most severely impacted on the southeast Upolu coast. The distribution and intensity of inundation is dependent on local topographic and bathymetric features, configuration of coastal geomorphology, and trapping of short-period waves over the reef flats. For one of the sources, comparison of the relative contributions of the normal and thrust faulting components of the doublet to the southeast Upolu inundation indicates that the initial intraplate normal faulting dominated the east-northeastward tsunami propagation and inundation compared with the subsequent interplate thrust faulting. Overall, two key source models are discussed and identified for future refinement.

Effects of source faulting and fringing reefs on the 2009 South Pacific tsunami inundation in southeast Upolu, Samoa

Cyprien Bosserelle[1], Shaun Williams[1], Kwok Fai Cheung[2], Thorne Lay[3], Yoshiki Yamazaki[2], Titimanu Simi[4]†, Volker Roeber[5], Emily Lane[1], Ryan Paulik[1], Lameko Simanu[4]

[1]National Institute of Water and Atmospheric Research (NIWA), New Zealand. [2]Department of Ocean and Resources Engineering, University of Hawaii at Manoa, Hawaii, USA. [3]University of California Santa Cruz, California, USA.[4] Management Office, Ministry of Natural Resources and Environment, Apia, Samoa. [5] de Pau et des Pays de l'Adour (UPPA), HPC-Waves Laboratoire SIAME, Pau, France.

Corresponding author: Cyprien.Bosserelle@niwa.co.nz

†Current affiliation: Management Unit, Green Climate Fund, Samoa Ministry of Finance.

Key Points:

- The tsunami water level produced by the 2009 earthquake doublet is simulated for Samoa and compared to observed runup on southeast Upolu.
- Geometry of the intraplate normal faulting near the northern Tonga Trench terminus influences the extreme runup on southeast Upolu.
- The runup on southeast Upolu is also dependent on fine-scale topographic features and wave excitation over the reef flats.

Abstract

The subduction zone along the northern Tonga Trench has the highest plate convergence rate in the world, but limited records of its seismic and tsunamigenic activities. In 2009, a tsunami generated by an M_W 8.1 earthquake doublet caused severe impacts in the region including damage and loss of life on the south shores of Upolu and Savaii Islands, Samoa. Here we use numerical modeling aided by recorded data and eyewitness accounts to evaluate which of the published source models in the Tonga Trench region most suitably represents the 2009 event for use in hazard assessment around Samoa. We show that only a few of the published sources are suitable to reproduce large inundation observed in Samoa and none reproduces runup as high as observed in areas that were most severely impacted on the southeast Upolu coast. The distribution and intensity of inundation is dependent on local topographic and bathymetric features, configuration of coastal geomorphology, and trapping of short-period waves over the reef flats. For one of the sources, comparison of the relative contributions of the normal and thrust faulting components of the doublet to the southeast Upolu inundation indicates that the initial intraplate normal faulting dominated the east-northeastward tsunami propagation and inundation compared with the subsequent interplate thrust faulting. Overall, two key source models are discussed and identified for future refinement.

Plain Language Summary

This study models the September 29, 2009 tsunami in Samoa and compares model outputs with tsunami water level observations, field data of runup and inundation as well as eye-witness accounts collected after the event occured. Whilst several studies have reconstructed the runup and inundation of this event in American Samoa, this is the first time such work has been undertaken in Samoa which lies to the west (formerly known as Western Samoa). We discuss the effects of the complex earthquake sequence that triggered the tsunami event, as well as influence

of nearshore coastal characteristics on the pattern and behavior of tsunami impacts observed onshore.

1 Introduction

Tsunami inundation in reef-fringed environments is highly influenced by the characteristics of the source event [e.g., *Li et al.,* 2016] as well as the nearshore geomorphology [e.g., *Tang et al.,* 2009; *Roeber et al.,* 2010; *Gelfenbaum et al.,* 2011; *Dilmen et al.,* 2018]. Local observations of nearshore and runup processes provide the evidence-base for refining and improving source parameters through forward tsunami modeling [e.g., *Yamazaki et al.,* 2018; *Davies,* 2019]. Such improvements can lead to more realistic tsunami hazard representations and a better understanding of local processes for use in coastal management planning.

The 29 September 2009 South Pacific Tsunami (SPT) initiated from an M_W 8.1 earthquake sequence involving nearly simultaneous intraplate normal faulting in the outer rise oceanic plate and major interplate reverse faulting (M_W 8.0) occurring within two minutes of the initial rupture [*Beavan et al.,* 2010; *Lay et al.,* 2010; *Kiser and Ishii,* 2012; *Fan et al.,* 2016; *Hossen at al.,* 2017]. The USGS-NEIC epicenter (15.489°S, 172.095°W) for this M_W 8.1 event is located 150 km east of the 1917 M_W ~8.0 event (Figure 1). The combined faulting generated a tsunami across the South Pacific that caused widespread inundation, damage and loss of life on the southern coasts of Upolu and Savaii Islands in the Independent State of Samoa (herein Samoa) , Tutuila Island in American Samoa, and Niuatoputapu Island in northern Tonga [*Okal et al.,* 2010; *Goff and Dominey-Howes,* 2011].

In the aftermath of the event, extensive investigation of the tsunami source and wave characteristics were undertaken based on seismic and GPS records, field surveys and numerical modeling [e.g., *Beavan et al.,* 2010; *Lay et al.,* 2010; *Okal et al.,* 2010; *Roeber et al.,* 2010; *Goff and Dominey-Howes,* 2011*; Yamazaki et al., 2011; Zhou et al.,* 2012; *Fan et al.,* 2016; *Hossen et al.,* 2017; *Dilmen et al.,* 2018; *Wood et al.,* 2018; *Han et al.,* 2019; *Williams,* 2019]. Previous

efforts to reconstruct tsunami characteristics in Samoa were limited to simulating wave initiation and dispersion up to the reef edge [e.g., *Fritz et al.*, 2011; *Okal et al*., 2011; *Franchello and Annunziato*, 2012; *Zhou et al*., 2012]. Shoreward wave propagation and inundation was not previously addressed due to lack of high-resolution topography and nearshore bathymetry for this region. Recent acquisition of high-resolution LiDAR topography and nearshore bathymetry [*FUGRO*, 2016] now enables re-evaluation of the event; modeling the tsunami initiation, propagation, and inundation along southeast Upolu, Samoa.

This paper reconstructs the 2009 SPT to study the characteristics of wave initiation, propagation and inundation in Samoa, with emphasis on the observed runup particularly on southeast Upolu Island. This coastline experienced the highest observed runup, flow depths, damage and loss of life [*Okal et al.*, 2010]. We assess whether current understanding of the rupture mechanism and propagation explains the extreme runup and flow depths observed in this region. We test rupture source mechanisms compiled by *Fan et al.* [2016], *Hossen et al.* [2017] and *Han et al.* [2019] against the Deep Ocean Assessment and Reporting of Tsunami (DART) data closest to the source, Apia tide gauge measurements, and runup measurements from post-disaster surveys [e.g. *Okal et al*., 2010, 2011; *Dudley et al.* 2011; *Reese et al.*, 2011].

We consider 14 source representations of the 2009 SPT that are obtained directly or adapted from published models. The overall objective is to identify which of the 14 source representations produce the most realistic inundation and runup for future refinement (e.g. in finite-fault models) and use in hazard exposure and impacts assessment. The importance of validating models with surveyed runup, as well as quantifying the effects of coastal topography on wave behavior, are discussed.

2 Regional context and setting

The Samoan archipelago comprised of Samoa and American Samoa is situated along a volcanic hotspot island chain [*Koppers et al*., 2008], located approximately 100 km north of the

terminus of the Tonga Trench. The tectonics and seismicity of this region are illustrated in Figure 1. The Pacific Plate undergoes strong deformation as it subducts steeply beneath the Tonga Arc, while north of the hook-like terminus the plate continues westward. The bending and tearing of the plate at the terminus [e.g., *Millen and Hamburger*, 1998; *Govers and Wortel*, 2005] coupled with mantle plume upwelling [e.g., *Koppers et al.*, 2011; *Konter and Jackson*, 2012; *Chang et al.*, 2016], produces complex strain and faulting that results in significant seismic hazard for the Samoan archipelago [e.g., *Gurnis et al.*, 2000; *Fan et al.*, 2016]. The average convergence rate of 25 cm/yr between the Pacific plate and the overriding Tonga block is the highest among all subduction zones [*Bevis et al*., 1995; *Basset et al.*, 2016]. The rate is enhanced by rapid back-arc spreading of the Lau Basin combined with roll-back of the subduction zone [*Chang et al.*, 2016].

Despite the high convergence and seismicity rate [*Basset et al.*, 2016], recorded interplate thrust faulting activity only involves events with magnitudes less than ~8.0 [e.g., *Meng et al*., 2015]. Intraplate earthquakes within the deformed Pacific Plate, such as the 26 June 1917 Samoa (M_m 8; M_S 8.7) and 2009 Samoa-Tonga earthquakes located along the bend in the arc (Figure 1), are the largest recorded seismic events in the region [e.g., *Okal*, 1992; *Meng et al*., 2015] and both have triggered major tsunamis [*Okal et al.*, 2011].

There is general agreement that the overall source of the 2009 SPT involved both interplate thrust-faulting and intraplate normal-faulting. *Beavan et al.* [2010] used campaign geodetic observations and approximate tsunami arrival time reports to infer that a slow tsunami-earthquake on the plate boundary interface triggered trench-slope intraplate normal-faulting. *Lay et al.* [2010] used regional and teleseismic waveform modeling to develop a model where intraplate normal-faulting occurred first, triggering interplate thrusting events 49 and 90 s after the initial rupture, with the timing of all large moment release well constrained by the seismic signals. Analysis of two-event centroid-moment tensor solutions by *Duputel et al.* [2012], *Nealy and Hayes*, [2015], and *Fan et al*. [2016] support the latter interpretation, but the possibility of a precursory weak, very long-duration initial slip event on the thrust plane has not been ruled out.

Modeling of seismic waves for the intraplate normal faulting has invoked either a southwestward dipping plane [e.g., *Lay et al*., 2010; *Nealy and Hayes*, 2015] or an east-northeastward dipping plane [e.g., *Li et al*., 2009; *Beavan et al*., 2010; *Nealy and Hayes*, 2015; *Fan et al*. 2016]. The latter orientation is compatible with modeling of the reconstructed tsunami source area [e.g., *Hossen et al*., 2017] and with models of geodetic and gravity changes including viscoelastic relaxation [e.g., *Han et al.*, 2019]. However, the precise strike and dip of either candidate fault plane is ambiguous because of frequency dependence of the long-period point-source moment tensors and their associated best-double couple fault plane candidates [*Lay et al*., 2010]. Modeling an eastward dipping normal fault implies an increased slab dip and dominance of the oceanic plate bending moment relative to decreased in-plane force, and greater extensional in-shear stress causing a negative dynamic topography response seaward of the trench axis [e.g., *Craig et al.*, 2014].

While detailed orientation and timing of the complex faulting is not fully resolved, there is agreement that the resulting tsunami was triggered by both normal and reverse faulting. *Roeber et al*. [2010] attributed the impacts of the tsunami along the shores of Tutuila Island (American Samoa), which lies approximately 97 km east of Upolu, to shelf resonance and tsunami amplification at the natural periods of bathymetric features. The near-shore bathymetry, generally characterized by steep slopes and narrow reef morphology on the insular shelf, was suggested to modulate the incident tsunami waves resulting in varying flow conditions around the island. *Wood et al.* [2018] later showed that multiple waves with similar amplitudes impacted most locations in American Samoa rather than a single large wave. Nevertheless, fringing reef morphology and narrow embayments are important factors in explaining the variations in runup and flow depth on Tutuila [*Roeber et al.*, 2010; *Gelfenbaum et al.*, 2011; *Dilmen et al.*, 2015,

143 2018]. In Samoa, such analysis of wave characteristics relative to the magnitude of inundation
144 observed has not previously been carried out and is the focus of this paper.

145 **3 Methods and Data**

146 **3.1 Model Configuration and Grid Scheme**

147 The shock-capturing hydrodynamics model BG-Flood (Block-adaptive on Graphics
148 processing unit Flood model) is used to reconstruct the 2009 tsunami from the seismic source to
149 inundation (Figure 2). BG-Flood simulates shallow water hydrodynamics on Graphics
150 Processing Units (GPU) using an Adaptive Mesh Refinement type grid. The model governing
151 equations are from the Saint-Venant, Shallow Water Equation (SWE) solver of Basilisk
152 [*Popinet,* 2011], but uses a Block Uniform Quadtree mesh that runs efficiently on the GPU [e.g.,
153 *Vacondio et al.,* 2017]. The SWE engine is well established and tested in Basilisk through
154 tsunami benchmark evaluation, with the solver and its ability to define propagation and
155 inundation described by *Popinet* [2012]. The model, however, does not include dispersive terms
156 (present in Boussinesq-type or non-hydrostatic models). While the model is well suited for
157 testing the range of source scenarios to identify which one/s provide the most representative
158 modelled to observed inundation and runup comparisons, it may not be capable of reproducing
159 some of the high frequency tsunami waves and their nearshore behavior.

160 The BG-Flood model is configured using three nested uniform Cartesian grids to simulate the
161 2009 tsunami propagation from initiation to inundation (Figure 2). The level-1 grid extends
162 across the northern region of the Tonga Subduction Zone at a resolution of 250 m to capture
163 DART 51425, DART 51426 and DART 54401, as well as wave propagation around the Samoan
164 Islands. The level-2 grid resolves wave inundation on Upolu, Manono (immediately west of
165 Upolu) and Savaii Islands at 50 m resolution for comparison with surveyed runup in these
166 islands [*Okal et al*. 2010] and includes the Apia tide gauge. The level-3 grid solves for
167 inundation at 10 m resolution on southeast Upolu for more detailed comparison with surveyed

168 runup in this area [*Okal et al.* 2010; *Reese et al.* 2011; *Dudley et al.* 2011]. The digital elevation
169 models (DEM) used in these simulations were derived from: 1) the Generic Bathymetric Chart of
170 the Oceans (GEBCO) at ~900 m resolution; 2) multi-beam bathymetry survey over the shelf
171 slopes at a resolution of ~60 m [*Kruger and Kramer* 2008]; and 3) Light Detection and Ranging
172 (LiDAR) topography and nearshore bathymetry (down to 30 m depth) at a resolution of 5 m
173 [*FUGRO,* 2016].

174 **3.2 Source Models, Observations Data and Comparison**

175 Instrumental records (DART buoys and tide gauge data) and runup measurements were
176 used to validate the tsunami simulations. Clear near-field signals of the 2009 SPT were recorded
177 at the three DART stations used in this study as well as the Apia tide gauge. Raw DART data
178 were processed using a Gaussian filter with a 216 s window; tsunami spectral density was
179 calculated from the filtered data resampled to a 10 s interval using the Welch's method with a
180 512 sample window.

181 For the Apia tide gauge, the tsunami signal was extracted by removing the tide signal from
182 recorded water level. The tide signal was first predicted using the T-tide software [*Pawlowicz et*
183 *al.* 2002], and using the full tide gauge record from 1993—2019.

184 Surveyed runup and flow depth were first converted to maximum water level for comparisons.
185 For the whole country analysis, 30 maximum water level points were used in Savai'i, 127 points
186 in Upolu and 7 points in Manono. For the southeast Upolu comparison, 65 maximum water level
187 points were available.

188 Fourteen source scenarios with different rupture parameters, timing, locations, angles, dips and
189 slip were simulated and compared with the open-ocean DART observations, Apia tide gauge
190 record and surveyed runup (Table 1). This includes a modified source, which applies the rupture
191 dimensions and slip of *Lay et al.* [2010] but with an east-northeast dipping normal fault [e.g.,

192 *Fan et al.*, 2016; *Hossen et al.*, 2016]. Fault 1 denotes the normal intraplate rupture in the outer
193 rise and faults 2 and 3 correspond to the later interplate thrusting on the plate boundary (Figure
194 2) (Table 1).

195 Source parameters include the rupture initiation and dislocation rise time to reconstruct the time
196 history of seafloor deformation through the half-space solutions of *Okada* [1985; 1992] for
197 modeling of tsunami generation. The intraplate rupture occurred below the 6000 m deep abyssal
198 seafloor , while the water depth above the thrust faulting extends from 2000 to 7000 m over the
199 margin. The 8300 m deep Tonga Trench lies between the locations of the two sub-events and
200 played a significant role in modifying the near-field tsunami through wave refraction associated
201 with rapid variation of the propagation speed. This suggests that the timing of rupture sequencing
202 and rise time (or rupture duration) are critical in accurately simulating the inundation.

203 To evaluate how each source configuration performs for wave propagation and inundation, wewe
204 compare the index of agreement between the modelled and observed tsunami wave signal at the
205 DART buoys and the Apia tide gauge. We also compare modelled and observed runup, first for
206 the entire country and then for southeast Upolu only. Each scenario was simulated from initiation
207 to propagation to the DART locations for a total of 4.2 hours for our level-1 grid. The country
208 inundation grid (level-2) and southeast Upolu grid (level-3) were also run for 4.2 hours. The
209 goodness of the fit between computed and observed maximum inundation (i.e., combined runup
210 and maximum flow elevation) is estimated using the Willmot index of agreement(Willmot 2012)
211 (Eq. 1):

212 $$IoA = \begin{cases} 1 - \frac{\sum_{i=0}^{n}|P_i - O_i|}{c\sum_{i=0}^{n}|O_i - \bar{O}|}, when\ \sum_{i=0}^{n}|P_i - O_i| \le c\sum_{i=0}^{n}|O_i - \bar{O}| \\ \frac{c\sum_{i=0}^{n}|O_i - \bar{O}|}{\sum_{i=0}^{n}|P_i - O_i|} - 1, when\ \sum_{i=0}^{n}|P_i - O_i| > c\sum_{i=0}^{n}|O_i - \bar{O}| \end{cases} \quad \text{(Eq. 1)}$$

213 where O_iO_i is the measured data, P_i is the simulated data, the over bar denotes the average, and
214 $c = 2$. As general guidance when comparing the complex nature of tsunami with idealized

simulation, a negative IoA is poor agreement, IoA<0.25 is weak agreement, IoA>0.5 is good agreement and IoA >0.8 is excellent agreement.

3.3 Simulation and Computation

The simulation applies the Apia tide level at the time of initiation but does not include the tide variation throughout the simulation. With the largest waves occurring within 15-20 min after the earthquake the tidal variation is not expected to influence the tsunami significantly. Each grid is nested one-way at a 1s interval. Outputs at the DART locations and Apia tide gauge are extracted at the model computational time step (~0.7 s at the DART buoys and ~0.1 s at the tide gauge). Maximum water level and flow depths are updated at each step and compared with observations data from *Okal et al.* [2010].

A uniform quadratic bottom roughness (cf = 0.0001) was applied to the 250 m and 50 m grids. A roughness formulation of *Smart* [2017] is used which is related to the Manning formulation but is also valid for very small flow depth without requiring a depth-dependent roughness length (z_0). A simple spatially varying roughness map with low roughness length (z_0 = 0.0001 m) was applied to elevations lower than 15 m below mean sea level, and a high roughness length (z_0 = 0.01 m) used for all other areas including coral reefs, vegetated land, and built environment. This is reasonable given the relatively low density of buildings and infrastructure along the southeast Upolu coastline.

4 Results and Interpretation

4.1 Comparison of different sources

The simulation of 14 different sources from tsunami generation to inundation provides a wide range of tsunami scenarios whose characteristics are compared with observations. The index of agreement of simulated tsunami against observation (Table 2) as well as visual

comparison of tsunami wave signal at DART buoys and tide gauge (Supporting Information S1-S14) are used to summarize the results.

None of the 14 sources produce excellent agreement (i.e. no IoA exceeds 0.8) and no sources produce consistently good agreement against all datasets (i.e. the DART data, the tide gauge and the runup data) (Table 2). Sources labeled *Lay et al.* [2010] Version D and E, as well as *Nealy & Hayes* [2015] Version T produce moderate to good agreements at the two closest DART buoys as well as the Apia tide gauge but do not reproduce observed runup in South East Upolu. On the other hand, *Lay et al.* [2010] Version C, a modified iteration of *Lay et al.* [2010] Version B for testing in this study, and *Hossen et al.* [2017] produces good agreement with observed runup but cannot reproduce the DART and tide gauge as well as other sources. With the DART buoys located far away from the main impact of the tsunami and recording waves in the order of 0.05 m, we deem it more important for a hazard assessment to better match the Apia tide gauge recording (~1. 0m tsunami) and runup (up to 15 m above mean sea level).

Overall *Hossen et al.* [2017] and *Lay et al.* [2010] Version C, while imperfect, are most consistent with the observed tsunami data. These two sources are discussed further in the sections below.

4.2 Propagation

BG-Flood simulates the full complexity of the rupture sequence in the tsunami generation to reconstruct the near-field wave pattern. The computed water levels for *Lay et al.* [2010] Version C are shown in Figure 3 at key moments after the rupture initiation time (see also Supporting Information Animation S15). The normal faulting generates a sea surface trough of 3 m heading to the northeast, while the uplift of the thrust faults adds to the southwest traveling positive wave from the normal fault to produce a surface pulse of 3.8 m amplitude. The relative position of the faults determines the radiated wave pattern across the ocean. The trough generated by the normal faulting reaches Upolu 11 min after the earthquake. It is immediately

followed by a positive wave from upswing of the initial surface depression and a larger and broader wave generated by the thrust faulting (Figure 3).

The second wave crest reaching the shore of southeast Upolu is augmented by reflection of the first to produce the highest water level 19 min after the earthquake, while standing waves gradually develop over the wider shelf to the west producing a large peak 9 min later. The wave pattern is reversed with a leading crest followed by a deep trough toward the west and south. The maximum surface elevation in Figure 3 shows a complex pattern with focusing of the waves behind islands and seamounts in the general propagation direction.

Tsunami simulations using both *Lay et al.* [2010] Version C and *Hossen et al.* [2017] adequately reproduces the arrival time at both DART locations and the tide gauge. Computed and recorded waveforms and spectra at the three DART buoys and the Apia tide gauge for these scenarios are shown in Figure 4, and compared in Figure 5. The amplitude of the DART observations are over-predicted, but because they are low amplitude, this is considered secondary. The waveform at Apia tide gauge is well modeled, but the amplitude is also overpredicted for this model. Comparisons for other models are shown in the Supporting Information S1-S14.

DART 51425 (northwest of the epicenter) and the Apia tide gauge (northeast of the epicenter) both recorded a leading trough from the normal faulting in the outer rise. At DART 51426 (southeast of the epicenter), a leading crest followed by a deep trough from the combined thrust and normal faulting was recorded. The validation of the DART and Apia tide gauge records corroborates the work of *Dilmen et al.* [2018] and *Wood et al.* [2018] in which a leading trough was observed at the Pago Pago Tide Gauge in Tutuila and at DART 51425 in the north, and a leading crest at DART buoys 51426 and 54401 south of the epicenter.

4.3 Computed and Recorded Inundation

Comparison between simulated and observed runup (Figure 6) shows the variable response of the tsunami along the shore. Some scenarios indeed produce high runup where observed. However, none of the 14 scenarios tested reproduce the extreme runup of 10-15 m on southeast Upolu. These extreme runups occurred East of Lepa, at the apex of Saleapaga bay and on the Lalomanu cliffs. Simulated maximum water levels show localized "spikes" in the runup located in the same area of the observed extreme runups suggesting that these were caused by highly localized amplification of the incoming tsunami wave..

Trapping and slow drainage of the initial wave within the narrow lagoon appear to provide a higher baseline for subsequent incoming waves to ride in on causing higher flow depths along this coast compared with other locations which were inundated. While southeast Upolu exhibits the highest overall runup in each scenario, the inability of any of the models to reproduce the extreme runup peaks suggests: 1) potential limitations of the DEM resolution in representing 2009 topography and bathymetry in the near- and on-shore; 2) complexity in the source mechanism which is not represented using uniform slip models (e.g., heterogenous slip); and/or 3) dispersive effect may be propagating waves with a period that better match the resonance mode of the location of extreme runup. Nevertheless). Nevertheless, the computed maximum runup for *Lay et al.* [2010] Version C and *Hossen et al.* [2017] scenarios are generally consistent with recorded observations on all three islands, and consistent with eye-witness accounts in southeast Upolu whereby the second and third waves were generally observed to be the largest [*Okal et al.*, 2011; *Dudley et al.*, 2011].

The simulation of *Lay et al.* [2010] Version C and *Hossen et al.* [2017] scenarios confirms the large variation observed in runups and flow depths along the shore as shown for Lepa and Saleapaga. At these locations, waves at the shoreline transform from a single peak reaching 6 m elevation at Saleapaga to a single peak of 4 m in Lepa 700 m to the west (Figure 7). A double

peak exceeding 5 m is observed 1000 m further west of Lepa. The waves around Saleapaga appear to have excited the local resonant frequencies over the reef flats [e.g., *Abe*, 2011], and showed the strongest onshore wave energy at these frequencies which is consistent with relatively high flow depths up to 6 m observed in this area (Figure 6b) [*Okal et al.*, 2010]. The strongest offshore energy signal observed at lower frequency from the initial pulse and higher onshore energy peaks at lower frequencies are probably due to interference and excitation over the reef flats and onshore [e.g. *Gelfenbaum et al.*, 2011; *Cheung et al*., 2013; *Gawehn et al.*, 2016; *Buckley et al.*, 2018].

5 Discussion

5.1 Complex source in complex bathymetry

The 2009 Samoa tsunami was unusual because it was triggered by an intraplate-interplate sequence of earthquake ruptures. The subsequent tsunami waves were transformed and trapped over complex bathymetric features significantly amplifying them as they reached and inundated the Samoan shoreline. The high resolution of the simulation presented here reveals the tsunami waves transformation as they reach the complex reef bathymetry.

While our modelling did not reproduce the extreme runup of 10-15 m observed on southeast Upolu, the highest modelled runups of ~ 9 m were exhibited on this coast. Extreme wave amplification and runup between Lalomanu and Salani on southeast Upolu is caused by very localized reef features (e.g. incisions and gullies) at the edge and inside of the narrow fringing reef morphology. These focus tsunami energy towards adjacent shorelines and exacerbated runup by trapping energy between the reef and the onshore cliff (Figure 8). Interference and convergence between reflected and incoming waves explain the local amplification and runup heights along the southeast coast. *Roeber et al*. [2010] and *Dilmen et al.* [2018] modelled similar amplifications due to nearshore reefs in Tutuila exciting resonant modes of 2-4 min on the insular shelf surrounding American Samoa. Our results show that the relative small change in the

335 incoming tsunami waves and interaction with the narrow reef morphology played a key role in
336 amplifying the 2009 SPT on southeast Upolu.

337 In general these observations support suggestions that high-frequency tsunami waves on reef
338 flats [e.g., *Gawehn et al.,* 2016], as well as geomorphologic configuration and fine-scale
339 topographic features within the reef system [e.g., *Gelfenbaum et al.,* 2011], are crucial local
340 drivers of extreme runup and coastal flooding. Furthermore, they support suggestions by *Baba et*
341 *al.* [2009] that narrow fringing reefs do not have the width to dissipate wave energy compared
342 with wider reefs. Although, in some circumstances, wider reefs may increase the wave height
343 through resonant interactions.

344 Interestingly, in the case of Lay et al. (2010) version C scenario, waves triggered by the normal
345 fault rupture alone can explain most of the large runup observed in most of southeast Upolu
346 (Figure 9). However, the normal fault alone can only explain 40 to 70 % of the maximum water
347 level offshore, and does not adequately account for the observed runup in Lepa or in the area
348 between Poutasi and Satalo, or the east-facing region of the coast. Longer wave periods
349 associated with the thrust rupture are amplified more significantly by the local bathymetry at
350 these locations compared with the shorter period waves produced by the normal fault. This
351 highlights how shorter tsunami waves get more easily trapped on narrow reefs and longer
352 tsunami waves are more easily trapped on wider reefs. Nevertheless, our observations
353 corroborate that tsunamis are highly sensitive to source parameters, with significant spatial
354 inundation variability for a given source. In addition, the observations suggest that 1-dimensional
355 tsunami attenuation modeling of offshore wave heights at coast, which is sometimes used to

356 estimate tsunami inundation hazard, is not adequate for use in reef fringed islands [e.g. *Smart et*
357 *al.,* 2015].

358 **5.2 Refinement of source mechanism**

359 Previous investigations of the 2009 tsunami source were unable to simulate inundation in
360 Samoa due to the lack of high resolution bathymetric and LiDAR topographic data. The analysis
361 presented in this study shows that each source generates a significantly different tsunami. The
362 *Lay et al.*[(2010] Version C and *Hossen et al.* [2017] sources produce the most consistent
363 agreement with tsunami records (observed runup in Upolu, Manono and Savaii and the recorded
364 at the Apia tide gauge and DARTs). However, the inability of any of the scenarios tested to
365 adequately capture the extreme runup (~14 m) observed at Lepa on southeast Upolu implies a
366 consistent deficiency in the sources tested.

367 This deficiency is unlikely to be resolved by testing additional uniform slip scenarios. For
368 example, decreasing the strike of the normal fault, could focus more energy and send larger
369 waves towards southeast Upolu, but this would also lead to larger waves reaching the Apia tide
370 gauge, worsening the agreement there. Doing so would also decrease the tsunami wave reaching
371 American Samoa. This would be inconsistent with previous findings that showed that even
372 simple sources involving only the normal fault could reproduce runup and tide gauge
373 measurement in Pago Pago [*Roeber et al*. 2010; *Dilmen et al.* 2018]. It is also likely that a
374 Boussinesq-type model will improve simulation of extreme runup. This will allow weakly
375 dispersive (high-frequency) waves to propagate from the source to Samoa and allow
376 amplification at these frequency to be captured at the coast.. These extreme runup could also be
377 due to swashing of the incoming wave or channeling of waves along gullies that are not
378 adequately represented in the DEM [e.g., *Smart et al.,* 2018] and 10 m model resolution. It is
379 also possible the LiDAR is not representative of pre-event landscape prior to post-disaster
380 reconstruction and modification of local topography. In this case, wave transformation over the

reef and trapping within the reef flats, which is dependent on local topography and a key driver of the observed runup, would not be adequately represented.

Heterogeneous rupture with variable slip distribution could also reconcile different issues in the scenarios used here. For example, a finite-fault model of the normal fault presented in *Lay et al.* [2010] could indicates larger slip patches west and east of the epicenter. This could provide additional tsunami energy towards Upolu while maintaining high tsunami energy towards Tutuila and limiting the amount of wave energy traveling to the Apia tide gauge in between the two islands. The higher frequency waves generated from a variable slip rupture may excite the resonance mode in Lepa and Lalomanu and might reproduce extreme runup. Hence, future investigation using a dispersive model and considering heterogeneous rupture with variable slip distribution, as well as stochastic source modeling and higher resolution simulation grid [*e.g. Li et al.,* 2016; *De Rissi and Goda,* 2017; *Yamazaki et al.,* 2018; *Davies et al.,* 2019], might improve the inundation and runup presented in this study.

Notwithstanding, the modelled inundation shows high spatial variability of runup and flow depths similar to surveyed observations, with areas of highest runup observed in southeast Upolu. Our results suggest variability is driven by the rupture source configuration and localized tsunami amplifications due to complex bathymetry within the fringing reef and along coastal topography.

This study highlights that good fits to the DART buoy data does not always guarantee accurate representation of runup, particularly where the buoys are situated away from the main tsunami energy beams. Nevertheless, the study demonstrates the use of tsunami runup simulation to model surveyed and instrumentally recorded coastal and deep-ocean observations to better constrain the event source. This approach, however, is highly reliant on available high-resolution topography and nearshore bathymetry data for tsunami-affected shorelines. Future LiDAR topography and bathymetry acquisition for the northern Tonga Islands could provide a basis to

re-evaluate the 2009 tsunami event following the above recommendation and and expand reconstruction of propagation and inundation to all three impacted island groups: Samoa, American Samoa, and northern Tonga. Using the runup information from all three countries would provide better constraints for validation of the finite-fault model of the tsunami source.

6 Conclusions

This study reconstructed the 2009 tsunami in Samoa to observe wave characteristics and evaluate the physical factors affecting the observed inundation in southeast Upolu. We applied BG-Flood to simulate the tsunami from initiation through propagation to inundation for 14 possible sources for the event and evaluated agreement against instrumental records and observed runup. Two source models performed better overall with moderate agreement with the DART and Apia tide gauge records, and good agreement with observed runup on Upolu, Manono and Savaii islands. While our model reproduces the runup along most of southeast Upolu (9 m), it does not capture the observed extreme value (14 m). We speculate that this is due to source complexities which are not represented using a uniform slip model, and limitations in the selected mode as well as the representativeness of near- and on-shore DEM. Analysis of the relative contributions of the normal and thrust faulting for this doublet event on tsunami behavior indicates that the normal fault alone can explain approximately 70% of the observed runup and flow depths up to 5 m on southeast Upolu.

Our findings indicate that inundation observed in Samoa is sensitive to the source rupture in addition to localized topographic and bathymetric features. The source details control the frequency contents of the tsunami and the fringing reefs control the resonance modes and periods. If the two constructively interfere, as was the case for the 2009 event along southeast Upolu, the impacts become much more severe than expected. The narrow fringing reef and constricted onshore geomorphology on southeast Upolu also plays a major role in exacerbating wave runup and flow depth along this coast. Future investigation and simulation of runup in all

three island groups impacted by the event (Samoa, American Samoa and Tonga) will enable iterative refinement of the source mechanism and nearshore effects to regional inundation distribution.

Acknowledgments, and Data

This research was supported by the New Zealand National Institute of Water and Atmospheric Research (NIWA), Strategic Science Investment Fund Project No. CARH2002, CARH2006 and PRAS2001 (SW, CB, RP, EL); U.S. National Oceanic and Atmospheric Administration Grant No. NA19NWS4670012 (KC, YY); TL's earthquake research was supported by the U.S. National Science Foundation (Grant EAR1802364). BG-Flood model is open-source and available at (https://github.com/CyprienBosserelle/BG_Flood), and the code version used in this research is archived at (http://doi.org/10.5281/zenodo.3905416). The supporting simulation video is available at (https://doi.org/10.5281/zenodo.4054271). LiDAR data were provided by the Samoa Ministry of Natural Resources and Environment (MNRE), Disaster Management Office through the Pacific Risk Tools for Resilience Project, and is available through MNRE via formal request. DART data used in this study were obtained from the U.S. National Oceanic and Atmospheric Administration, National Geophysical Data Center website: https://www.ngdc.noaa.gov/hazard/dart/2009samoa_dart.html. Tide gauge data was obtained from the Australian Bureau of Meteorology, Tides Unit through the Pacific Sea Level & Geodetic Monitoring project as part of Climate & Oceans Support Program in the Pacific also available from the U.S. National Tsunami Warning Center (https://ntwc.ncep.noaa.gov/previous.events/?p=09-29-09-Samoa). We thank the two anonymous reviewers for their helpful feedback which improved the paper. This study utilized the Generic Mapping Tools (GMT) for data processing and presentation. The authors declare that there are no real or perceived financial conflicts of interests associated with this research.

References

Abe, K. (2011), Synthesis of a Tsunami Spectrum in a Semi-Enclosed Basin Using Its Background Spectrum, *Pure Appl. Geophys*., *168*, 1101-1112, doi:10.1007/s00024-010-0222-x.

Baba, T., D. Burbidge, P. Cummins, and H. Thio (2009), The Effect of the Great Barrier Reef on the Propagation of the 2007 Solomon Islands Tsunami Recorded in Northeastern Australia. *Pure Appl. Geophys., 165*, doi:10.1007/s00024-008-0418-5.

Bassett, D., H. Kopp, R. Sutherland, S.A. Henrys, A.B. Watts, C. Timm, M. Scherwath, I. Grevemeyer, and C.E.J. de Ronde (2016) Crustal structure of the Kermadec Arc from MANGO seismic refraction profiles. *J. Geophys. Res. Solid Earth, 121*(10), 7514-7546, doi:10.1002/2016JB013194.

Beavan, J., X. Wang, C. Holden, K. Wilson, W. Power, G. Prasetya, M. Bevis, and R. Kautoke (2010), Near-simultaneous great earthquakes at Tongan megathrust and outer rise in September 2009, *Nature*, *466*, 959-963.

Bevis, M., F.W. Taylor, B.E. Schutz, J. Recy, B.L. Isacks, S. Helu, R. Singh, E. Kendrick, J. Stowell, B. Taylor, and S. Calmant (1995), Geodetic observations of very rapid convergence and back-arc extension at the Tonga arc, *Nature, 374*, 249-251, doi:10.1038/374249a0.

Buckley, M., R. Lowe, J. Hansen, A. van Dongeren, and C. Storlazzi (2018), Mechanisms of Wave-Driven Water Level Variability on Reef-Fringed Coastlines. *J. Geophys. Res., Oceans, 123*, 3811-3831, doi:10.1029/2018JC013933.

Chang, S.-J., A. Ferreira, and M. Faccenda (2016), Upper- and mid-mantle interaction between the Samoan plume and the Tonga–Kermadec slabs, *Nature Communications*, 7, doi:10.1038/ncomms10799.

Cheung, K.F., Y. Bai, and Y. Yamazaki (2013), Surges around the Hawaiian Islands from the 2011 Tohoku tsunami, *J. Geophys. Res., Oceans*, *118*(10), 5703-5719, doi: 10.1002/jgrc.20413.

Craig, T., A. Copley, and J. Jackson (2014), A reassessment of outer-rise seismicity and its implications for the mechanics of oceanic lithosphere, *Geophys. J. Int.*, *197*(1), doi:10.1093/gji/ggu013.

Davies, G. (2019), Tsunami variability from uncalibrated stochastic earthquake models: Tests against deep ocean observations 2006-2016, *Geophys. J. Int.,* 218, 1939-1960, doi:10.1093/gji/ggz260.

De Risi, R., and K. Goda (2017), Simulation-Based Probabilistic Tsunami Hazard Analysis: Empirical and Robust Hazard Predictions, *Pure Appl. Geophysc., 174*, 3083-3106, doi:10.1007/s00024-017-1588-9.

Dilmen, D., G. Roe, Y. Wei, and V. Titov (2018), The Role of Near-Shore Bathymetry During Tsunami Inundation in a Reef Island Setting: A Case Study of Tutuila Island, *Pure Appl. Geophys*., *175*, doi:10.1007/s00024-018-1769-1.

Dilmen, D., V. Titov, and G. Roe (2015), Evaluation of the Relationship Between Coral Damage and Tsunami Dynamics; Case Study: 2009 Samoa Tsunami. *Pure Appl. Geophys*., *172*, doi:10.1007/s00024-015-1158-y.

Dudley, W., R. Whitney, J. Faasisila, S. Fonolua, A. Jowitt, and M. Chan-Kau (2011), Learning from the victims: New physical and social science information about tsunamis from victims of the September 29, 2009 event in Samoa and American Samoa, *Earth-Science Reviews, 107*, 201-206, doi:10.1016/j.earscirev.2011.03.005.

499 Duputel, Z., H. Kanamori, V.C. Tsai, L. Rivera, L. Meng, J.-P. Ampuero, and J.M. Stock (2012),
500 The 2012 Sumatra great earthquake sequence, *Earth Planet. Sci. Lett., 351–352*, 247–257,
501 doi:10.1016/j.epsl.2012.07.017.

502 Fan, W., P.M. Shearer, C. Ji, and D. Bassett (2016), Mulitple branching rupture of the 2009 Tonga-
503 Samoa earthquake, *J. Geophys. Res. Soild Earth, 121*, 5809-5827,
504 doi.org/10.1002/2016JB012945.

505 Franchello, G., and A. Annunziato (2012), The Samoa Tsunami of 29 September 2009 – Early
506 Warning System and Inundation Assessment, *Sci. Tsu. Haz., 31*(1), 19-61, ISSN 8755-6839.

507 Fritz, H.M., J.C. Borrero, C.E. Synolakis, E.A. Okal, R. Weiss, V.V. Titov, B.E. Jaffe, S. Foteinis,
508 P.J. Lynett, I.-C. Chan, and P.L.-F. Liu (2011), Insights on the 2009 South Pacific tsunami in
509 Samoa and Tonga from field surveys and numerical simulations, *Earth-Science Reviews, 107,*
510 66-75, doi:10.1016/j.earscirev.2011.03.004.

511 FUGRO. (2016), Report of Survey: Airborne Lidar Bthymetric and Topographic Survey of Samoa
512 2015, Contract: ECRCR-LIB 2.1, Fugro LADS Document Reference No: TLCS00.047.008,
513 Issue No: 1.00, *Fugro LADS Corporation Pty Ltd*, South Australia.

514 Gawehn, M., A. van Dongeren, A. van Rooijen, C.D. Storlazzi, O.M. Cheriton, and A. Reniers
515 (2016), Identification and classification of very low frequency waves on a coral reef flat, *J.*
516 *Geophys. Res. Oceans*, *121*, 7560–7574, doi:10.1002/2016JC011834.

517 Gelfenbaum, G., A. Apotsos, A. Stevens, and B. Jaffe (2011), Effects of fringing reefs on tsunami
518 inundation: American Samoa, *Earth-Science Reviews,* 107, 12-22,
519 doi:10.1016/j.earscirev.2010.12.005.

520 Goff, J., and Dominey-Howes, D., (Eds.). (2011), The 2009 South Pacific Tsunami, *Earth-Science*
521 *Reviews, 107*, doi.org/10.1016/j.earscirev.2011.03.006.

522 Govers, R., and M. Wortel (2005), Lithosphere tearing at STEP faults: response to edges of
523 subduction zones, *Earth Planet. Sci. Lett., 236*(12), 505-523, doi:10.1016/j.epsl.2005.03.022.

524 Gurnis, M., J. Ritsema, H.J. Van Heijst, and S. Zhong (2000), Tonga slab deformation: the
525 influence of a lower mantle upwelling on a slab in a young subduction zone. *Geophys. Res.*
526 *Lett.*, *27*, 2373–2376, doi: 10.1029/2000GL011420.

527 Han, S.-C., J. Sauber, F. Pollitz, and R. Ray (2019) Sea Level Rise in the Samoan Islands Escalated
528 by Viscoelastic Relaxation After the 2009 Samoa-Tonga Earthquake, *J. Geophys. Res.*, *Solid*
529 *Earth, 124*(4), 4142—4156, doi:10.1029/2018JB017110.

530 Hossen, J., A. Gusman, K. Satake, and P. Cummins (2017), An Adjoint Sensitivity Method
531 Applied to Time Reverse Imaging of Tsunami Source for the 2009 Samoa Earthquake,
532 *Geophys. Res. Lett., 45*(2), 627-636, doi:10.1002/2017GL076031.

533 Kiser, E., and M. Ishii (2012), Combining seismic arrays to image the high-frequency
534 characteristics of large earthquakes, *Geophys. J. Int., 188*(3), 1117-1128, doi:10.1111/j.1365-
535 246X.2011.05299.x.

536 Konter, J., and M. Jackson (2012), Large volumes of rejuvenated volcanism in Samoa: Evidence
537 supporting a tectonic influence on late-stage volcanism, *Geochem. Geophys. Geosyst., 13*,
538 Q0AM04, doi:10.1029/2011gc003974.

539 Koppers, A.A.P., J. Russell, M.G. Jackson, J. Konter, H. Staudigel, and S.R. Hart (2008), Samoa
540 reinstated as a primary hotspot trail, *Geology, 36*(6), 435-438, doi:10.1130/G24630A.1.

541 Koppers, A.A.P., J.A. Russell, J. Roberts, M.G. Jackson, J.G. Konter, D.J. Wright, H. Staudigel,
542 and S.R. Hart (2011), Age systematics of two young en echelon Samoan volcanic trails,
543 *Geochem. Geophys. Geosyst., 12*, Q07025, doi:10.1029/2010GC003438.

Kowalik, Z (2011), Depth-integrated, non-hydrostatic model with grid nesting for tsunami generation, propagation, and run-up. *Int. J. Num. Meth. Fluids*, 67(12), 2081-2107.

Krüger, J., and S. Kumar (2008), Samoa Technical Report: High-resolution Bathymetric Survey. EU-SOPAC Project Report ER 112, Pacific Islands Applied Geoscience Commission, Suva, Fiji.

Lay, T., C.J. Ammon, H. Kanamori, L. Rivera, and K.D. Koper (2010), The 2009 Samoa-Tonga great earthquake triggered doublet, *Nature*, *466*, 964-968, doi:10.1038/nature09214.

Li, X., G. Shao, and C. Ji (2009), Rupture process of Mw 8.1 Samoa earthquake constrained by joint inverting teleseismic body, surface waves and local strong motion, *EOS Trans*., AGU, *90*(53), U21D-03.

Li, L., T. Lay, K.F. Cheung, and L. Ye (2016), Joint modeling of teleseismic and tsunami wave observations to constrain the 16 September 2015 Illapel, Chile Mw 8.3 earthquake rupture process, *Geophys. Res. Lett.*, *43*(9), 4303-4312, doi:10.1002/2016GL068674.

Meng, Q., D.S. Heeszel, L. Ye, T. Lay, D.A. Wiens, M. Jia, and P.R. Cummins (2015), The 3 May 2006 (M_W 8.0) and 19 March 2009 (M_W 7.6) Tonga earthquakes: Intraslab compressional faulting below the megathrust, *J. Geophys. Res., Solid Earth*, *120*, 6297-6316, doi:10.1002/2015JB012242.

Millen, D.W., and M.W. Hamburger (1998), Seismological evidence for tearing of the Pacific plate at the northern termination of the Tonga subduction zone, *Geology*, *26*(7), 659-662, doi:10.1130/0091-7613.

Nealy, J.L., and G.P. Hayes (2015), Double point source W-phase inversion: Real-time implementation and automated model selection, *Phys. Earth Planet. Inter.*, *249*, 68–81, doi:10.1016/j.pepi.2015.09.005.

Okada, Y. (1985), Surface deformation due to shear and tensile faults in a half space. *Bull. Seismol. Soc. Am.*, *75*(4), 1135-1154.

Okal, E. (1992), Use of the mantle magnitude *Mm* for the reassessment of the moment of historical earthquakes, I: Shallow events, *Pure Appl. Geophys.*, *139*, 17-57.

Okal, E., J. Borrero, and C. Chagué-Goff (2011), Tsunamigenic predecessors to the 2009 Samoa earthquake, *Earth-Sci. Rev.*, *107*, 127-140.

Okal, E.A., H.M. Fritz, C.E. Synolakis, J.C. Borrero, R. Weiss, P.J. Lynett, V.V. Titov, S. Foteinis, B.E. Jaffe, P.L.-F. Liu, and I.-C. Chan (2010), Field Survey of the Samoa Tsunami of 29 September 2009. *Seismol. Res. Lett.*, *81*(4), 577-591.

Pawlowicz, R., B. Beardsley, S. Lentz (2002), Classical tidal harmonic analysis with error analysis in MATLAB using T_TIDE. *Computers & Geosciences*, *28*, 929-937, doi:10.1016/S0098-3004(02)00013-4.

Popinet, S. (2011), Quadtree-adaptive tsunami modeling , *Ocean Dynamics*, *61*(9), 1261-1285, doi:10.1007/s10236-011-0438-z.

Popinet, S. (2012), Adaptive modeling of long-distance wave propagation and fine-scale flooding during the Tohoku tsunami, *Nat. Haz. Earth Sys. Sci.*, *12*(4), 1213-1227, doi:10.5194/nhess-12-1213-2012.

Reese, S., B.A. Bradley, J. Bind, G. Smart, W. Power, and J. Sturman (2011), Emprical building fragilities from observed building damage in the 2009 South Pacific tsunami, *Earth-Science Reviews*, *107*, 156-173, doi:10.1016/j.earscirev.2011.01.009.

Roeber, V., Y. Yamazaki, and K.F. Cheung (2010), Resonance and impact of the 2009 Samoa tsunami arounnd Tutuila. *Geophys. Res. Lett.*, *37*, L21604, doi:10.1029/2010GL044419.

589 Smart, G. (2017), Improving Flood Hazard Prediction Models, *Int. J. River Basin Manag., 16,*
590 449-456, doi:10.1080/15715124.2017.1411923.

591 Smart, G. (2018), LiDAR resolution for catchment-inclusive hydrodynamic models, *River Flow*
592 *2018, E3S Web of Conferences, 40,* 06031, doi:10.1051/e3sconf/20184006031.

593 Smart, G., K. Crowley, and E. Lane (2015), Estimating tsunami run-up. *Nat. Hazards, 80,*
594 doi:10.1007/s11069-015-2052-8.

595 Tang, L., V. Titov, and C. Chamberlin (2009), Development, testing, and applications of site-
596 specific tsunami inundation models for real-time forecasting, *J. Geophys. Res., Atmosphere,*
597 *114*, doi:10.1029/2009JC005476.

598 Vacondio, R., A. Palù, A. Ferrari, P. Mignosa, F. Aureli, and S. Dazzi (2017), A non-uniform
599 efficient grid type for GPU-parallel Shallow Water Equations models, *Environ. Modell. Softw*.,
600 *88,* 119-137, doi:10.1016/j.envsoft.2016.11.012.

601 Williams, S. (2019), Tsunami Elemental Signatures in the Samoan Islands: A Case Study, In, L.F.
602 Mazadiego, E.D.M. Garcia, F. Barro-Parra, and M. Izquierdo-Díaz, Applied Geochemistry with
603 Case Studies on Geological Formations, Exploration Techniques and Environmental Issues,
604 *InTech Open*, doi:10.5772/intechopen.85639.

605 Willmott, C., S. Robeson, K. Matsuura (2012), A refined index of model performance. *Int. J.*
606 *Climatol*., *32,* doi:10.1002/joc.2419.

607 Wood, N., J. Jones, Y. Yamazaki, K.F. Cheung, J. Brown, J. Jones, and N. Abdollahian (2018),
608 Population vulnerability to tsunami hazards informed by previous and projected disasters: a
609 case study of American Samoa. *Nat. Hazards*, doi:10.1007/s11069-018-3493-7.

610 Yamazaki, Y., K.F. Cheung, and T. Lay (2018), A self-consistent fault-slip model for the 2011
611 Tohoku earthquake and tsunami, *J. Geophys. Res., Solid Earth*, *123*(2), 1425-1458, doi:
612 10.1002/2017JB014749

613 Zhou, H., Y. Wei, and V.V. Titov (2012), Dispersive modeling of the 2009 Samoa tsunami,
614 *Geophys. Res. Lett*., *39*, L16603, doi:10.1029/2012GL053068

615 **Table 1.** Fault parameters for the main scenarios tested for runup in southeast Upolu. Fault
616 parameters from original publications (length, width and slip) have been modified to produce
617 comparable output.

No.*	Length (km)	Width (km)	Strike angle (º)	Dip angle (º)	Rake angle (º)	Slip (m)	Centroid of rupture			Rupture initiation (sec)**	Rise time (sec)
							Depth (km)	Long. (ºW)	Lat. (ºS)		
Li et al. (2009)											
1	130	50	340.7	45.4	-46.3	4.3	12	172.5	15	15.7	46.6
2	50	50	183.7	13.9	69.3	15.8	10	172.5	16.1	91.6	50.8
Beaven et al. (2010)											
1	130	50	352	53	-32	3.1	12	172.2	15.5	0.0	0.0
2	50	50	173	16	75	11.2	12	172.8	16	30	20
Lay et al. (2010) (Version A)											
1	130	50	152.0	67.0	-77.0	6.1	18	172.0	15.5	3.0	60.0
2	50	50	185.0	29.0	90.0	5.6	18	172.4	16.0	49.0	40.0
3	50	50	185.0	29.0	90.0	5.6	18	172.4	16.0	90.0	40.0
Lay et al. (2010) (Version B)											
1	130	50	144.0	65.0	-91.0	6.1	18	172.0	15.5	3.0	60.0
2	50	50	185.0	29.0	83.0	4.7	18	172.3	15.8	49.0	40.0
3	50	50	185.0	29.0	83.0	4.4	18	172.3	16.0	90.0	40.0
Lay et al. (2010) (Version C)											
1	130	50	324.0	65.0	-85.0	10.2	18	172.0	15.5	3.0	60.0
2	50	50	175.0	29.0	90.0	4.7	18	172.4	16.0	49.0	40.0
3	50	50	180.0	29.0	90.0	4.7	18	172.4	16.0	90.0	40.0
Lay et al. (2010) (Version D)											
1	110	35	340	35	265	6.0	15.2	172.00	15.50	3.0	60.0
2	50	75	175	20	90	4.62	17.8	172.70	15.78	49.0	40.0
3	50	75	180	20	90	4.71	17.8	172.68	16.27	90.0	40.0
Lay et al. (2010) (Version E)											
1	110	35	320	35	265	6.0	15.2	172.00	15.50	3.0	60.0
2	50	75	175	20	90	4.62	17.8	172.70	15.78	49.0	40.0
3	50	75	180	20	90	4.71	17.8	172.68	16.27	90.0	40.0
Duputel et al. (2012)											
1	130	50	157.0	64.0	-70.0	4.8	16	172.2	15.1	32.4	53.6
2	50	50	176.9	10.9	79.4	13.3	16	172.7	16.3	105.4	40.0
Nealy & Hayes (2015) (Version F)											
1	130	50	349.9	45.9	-84.6	9.2	16	172.2	15.2	33.0	66.0
2	50	50	158.1	39.6	51.7	19.5	16	172.2	15.2	45.0	80.0
Nealy & Hayes (2015) (Version U)											
1	130	50	356.0	40.1	-78.5	9.6	31	171.8	15.6	33.0	66.0
2	50	50	162.4	47.1	57.9	20.2	24	171.9	15.5	45.0	80.0
Nealy & Hayes (2015) (Version T)											

1	130	50	330.0	44.0	-81.0	4.3	18	172.1	15.5	25.0	50.0
2	50	50	178.5	18.0	59.0	14.3	18	172.9	16.4	91.0	182.0
Nealy & Hayes (2015) (Version C)											
1	130	50	153.0	61.5	-81.6	4.8	18	171.9	15.4	3.0	60.0
2	50	50	171.3	23.5	51.1	12.0	18	172.2	15.5	49.0	40.0
Fan et al. (2016)											
1	130	50	344.0	72.0	-68.0	4.3	12	172.2	15.0	0.0	70.0
2	50	50	183.0	15.0	40.0	15.8	12	172.5	16.1	80.0	80.0
Hossen et al. (2017)											
1	130	50	315.0	25.0	-99.0	6.1	18	172.0	15.5	3.0	60.0
2	50	50	180.0	29.0	90.0	7.9	18	172.4	16.0	49.0	40.0

618 * Fault 1 normal fault; Fault 2 reverse fault; Fault 3 reverse fault.

619 ** Initial rupture in seconds after the earthquake time (2009-09-29 17:48:10 UTC).

620

621
622 **Table 2**. Evaluation of the main scenarios against offshore and nearshore tsunami
623 observations. The evaluation is given as a correlation coefficient calculated as in Eq.1
624

Study	DART-51425	DART-51426	DART-54401	Apia tide Gauge	Samoa Runup	South-east Upolu runup
Li et al. (2009)	0.27	0.33	0.43	0.47	0.52	0.23
Beaven et al. (2010)	0.36	0.4	0.41	0.55	0.4	0.13
Lay et al. (2010) (Version A)	0.33	0.39	0.46	0.16	0.56	0.35
Lay et al. (2010) (Version B)	0.37	0.44	0.47	0.36	0.61	0.40
Lay et al. (2010) (Version C)	0.21	0.14	0.2	0.22	0.67	0.56
Lay et al. (2010) (Version D)	0.48	0.48	0.47	0.49	0.45	0.14
Lay et al. (2010) (Version E)	0.48	0.47	0.46	0.41	0.6	0.37
Duputel et al. (2012)	0.25	0.36	0.40	0.36	0.51	0.19
Nealy & Hayes (2015) (Version F)	-0.21	0.10	0.36	0.26	0.51	0.61
Nealy & Hayes (2015) (Version U)	0.13	0.13	0.42	0.42	0.64	0.55
Nealy & Hayes (2015) (Version C)	0.21	0.28	0.43	0.54	0.5	0.20
Nealy & Hayes (2015) (Version T)	0.33	0.37	0.35	0.30	0.45	0.17
Fan et al. (2016)	0.18	0.17	0.39	0.40	0.56	0.24
Hossen et al. (2017)	0.38	0.41	0.49	0.25	0.63	0.52

625

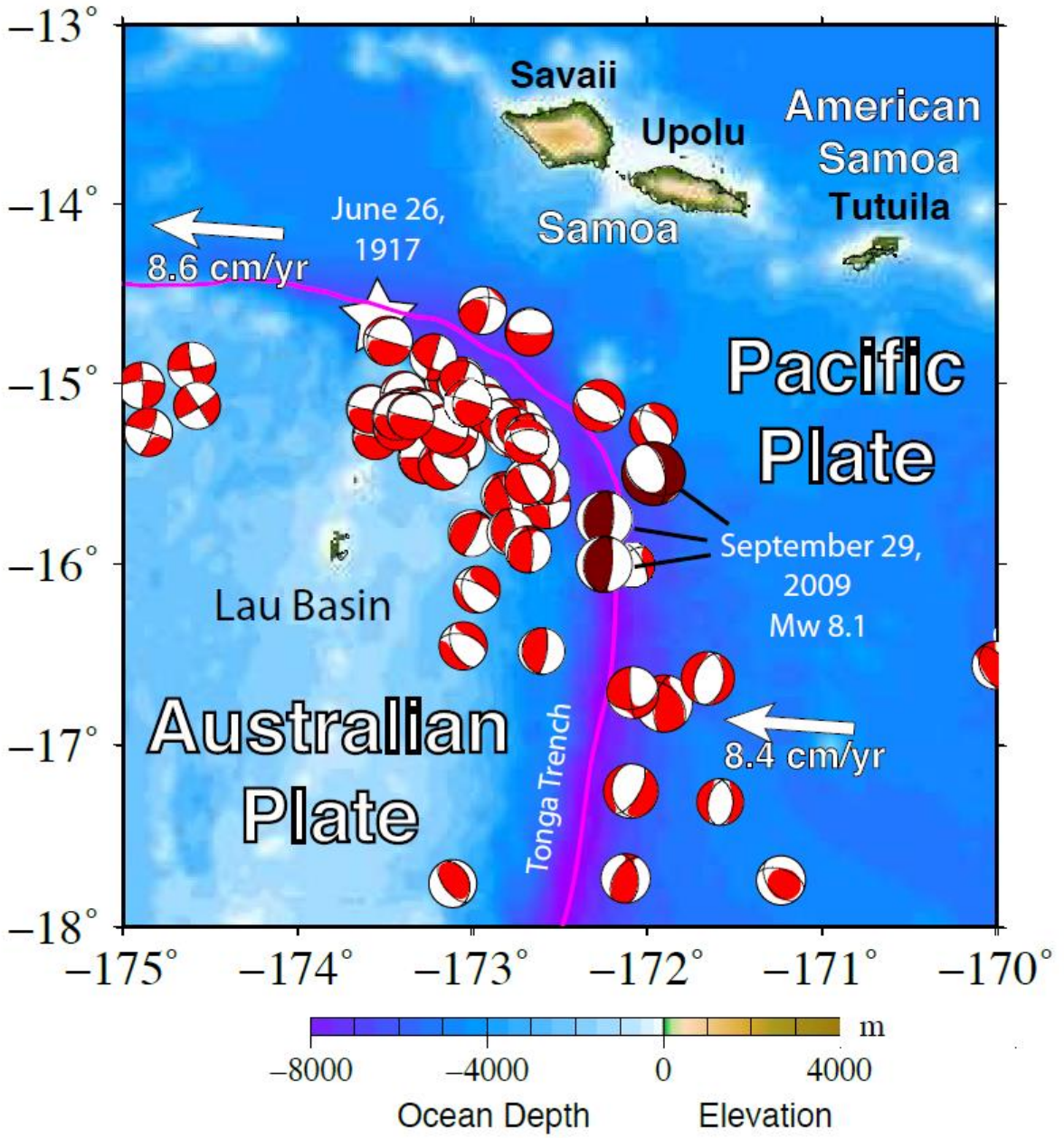

Figure 1. The northern Tonga subduction zone and the major Samoan Islands. The Pacific Plate underthrusts the Tonga block of the Australian Plate along the Tonga Trench. Spreading of the Lau Basin back-arc increases the convergence rate across the Tonga Trench to about 25 cm/yr in this region. The moment tensor solutions from the Global Centroid Moment Tensor catalog for $M_W \geq 6.0$ from 1976-2020 are shown. The star indicates the estimated location of the June 26, 1917 ($M_W \sim 8.0$) earthquake (ISC-GEM). The September 29, 2009 event involved an M_W 8.1 outer-rise normal faulting and two interplate thrust faulting events with a combined M_W 8.0 [*Lay et al.*, 2010].

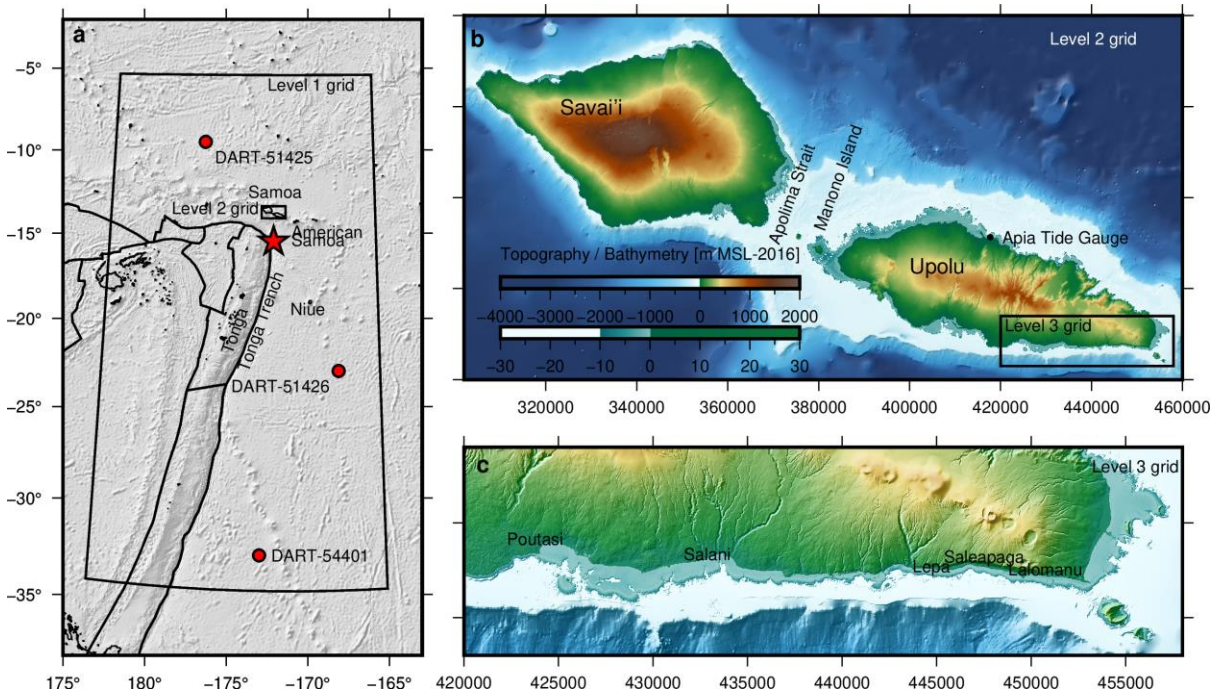

Figure 2. The model region for the 2009 South Pacific Tsunami. (a) Regional view with level-1 (250 m resolution) and level-2 (50 m resolution) computational domain outlined in black and DART buoy locations (red circles). Red star indicates epicenter. Rupture area of the 3 faults is delineated in white, with locations for faults 2 and 3 overlapping. (b) Level-2 computational domain showing the insular shelves of the Samoan Islands, the Apia tide gauge, and outline of the level-3 computational domain. (c) Level-3 computational domain showing the nearshore fringing reef system within the insular shelves on southeast Upolu.

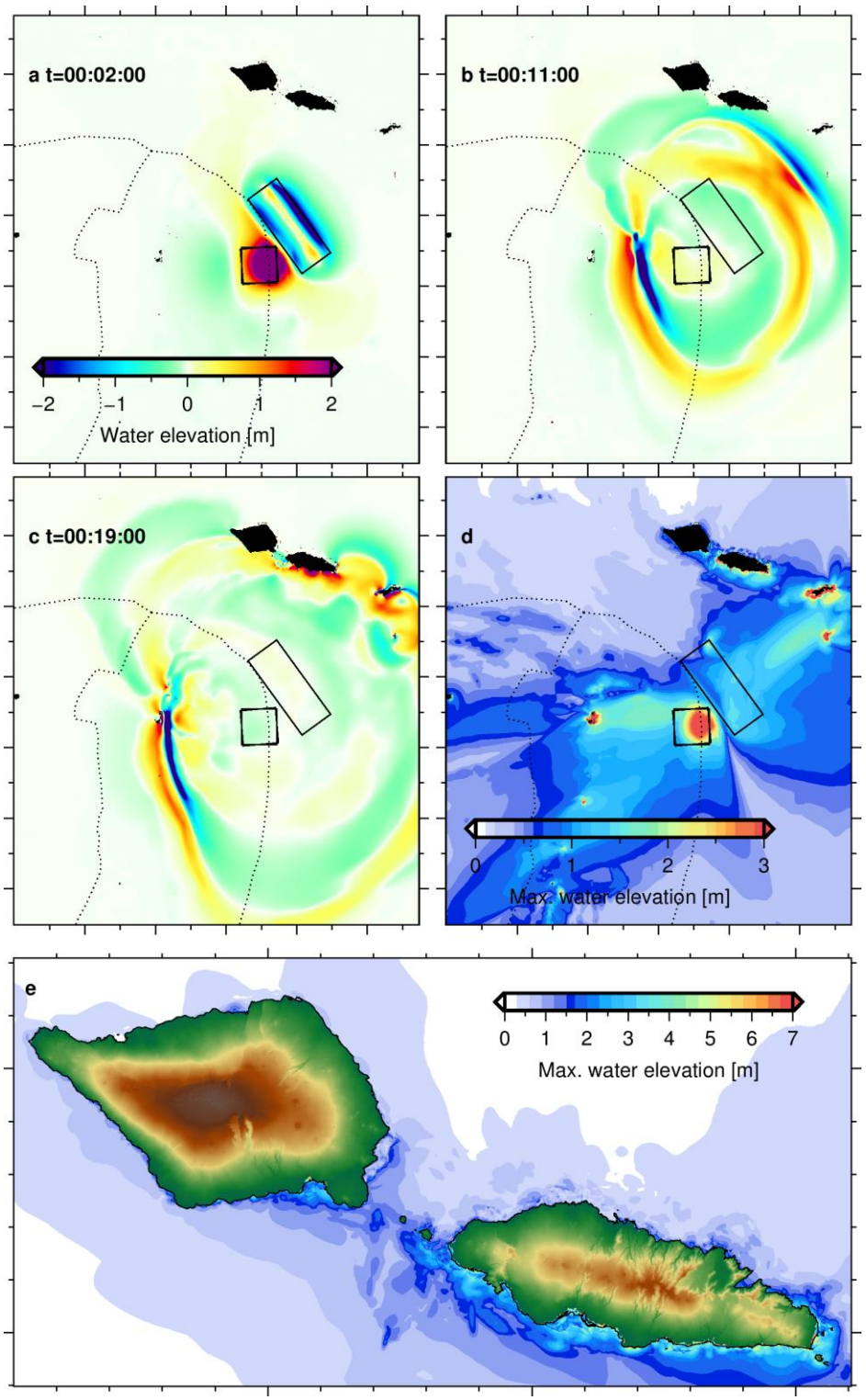

Figure 3. Snapshots of computed sea surface elevation after earthquake initiation, regional maximum surface elevation and inundation. The relative position of the initial surface disturbances gives rise to a trough leading the tsunami waves toward the north and east and a leading crest to the west and south. (a) Completion of the 3-fault rupture sequence (fault 2 and 3 have overlapping locations) note the wave generated from the normal fault is already bouncing back to a positive wave and the thrust faulting adding to the initial crest of the normal fault. (b) Arrival of the leading trough at coast on southeast Upolu. (c) Arrival of the combined first crest at coast on southeast Upolu. (d) Regional maximum water level. (e) Maximum inundation in the Samoan islands at 50m resolution.

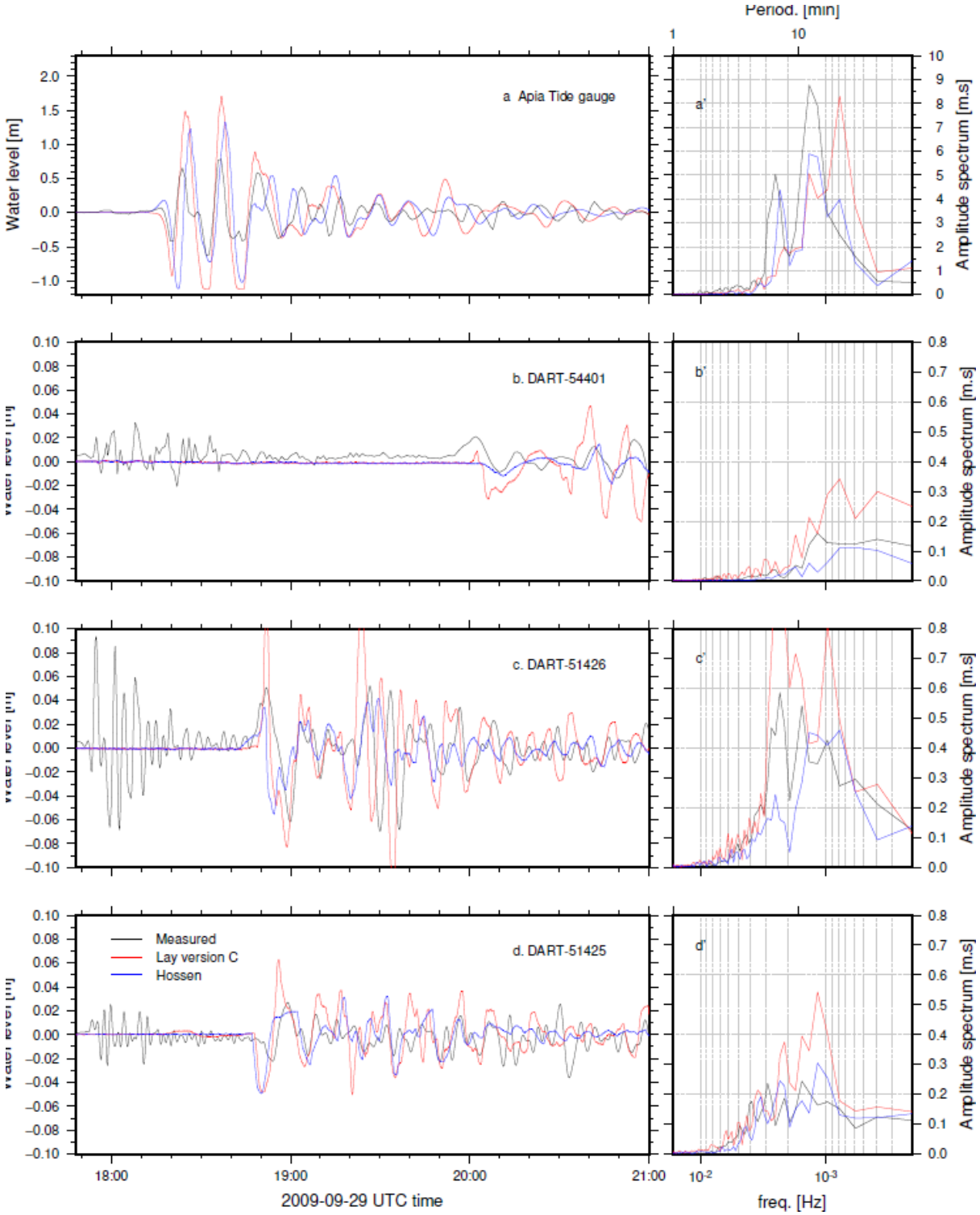

Figure 4. Comparison of recorded (black) and computed (red and blue) time series and spectra of surface elevations at DART water-level stations and the Apia tide gauge. The model reproduces the leading trough at DART 51425 to the north and the leading crest at DART 51426 to the south to confirm the two-stage rupture sequence. Simulated and recorded spectral amplitude is reasonably similar in all four gauges.

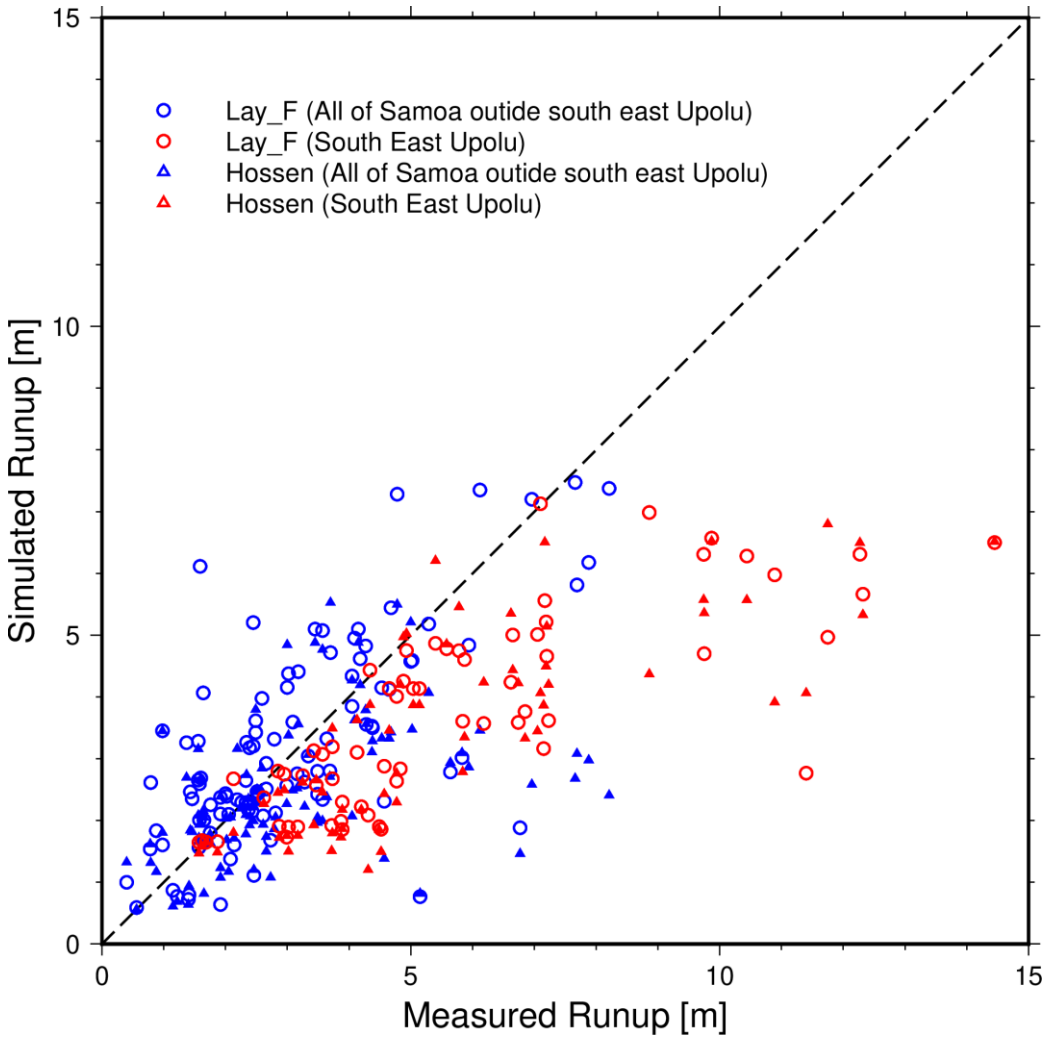

Figure 5. Comparison of measured and computed runup for the whole of Samoa (blue symbols) and southeast Upolu (red symbols) for the two scenario *Hossen et al.* [2017] (triangles) and *Lay et al.* [2010] version C (circles).

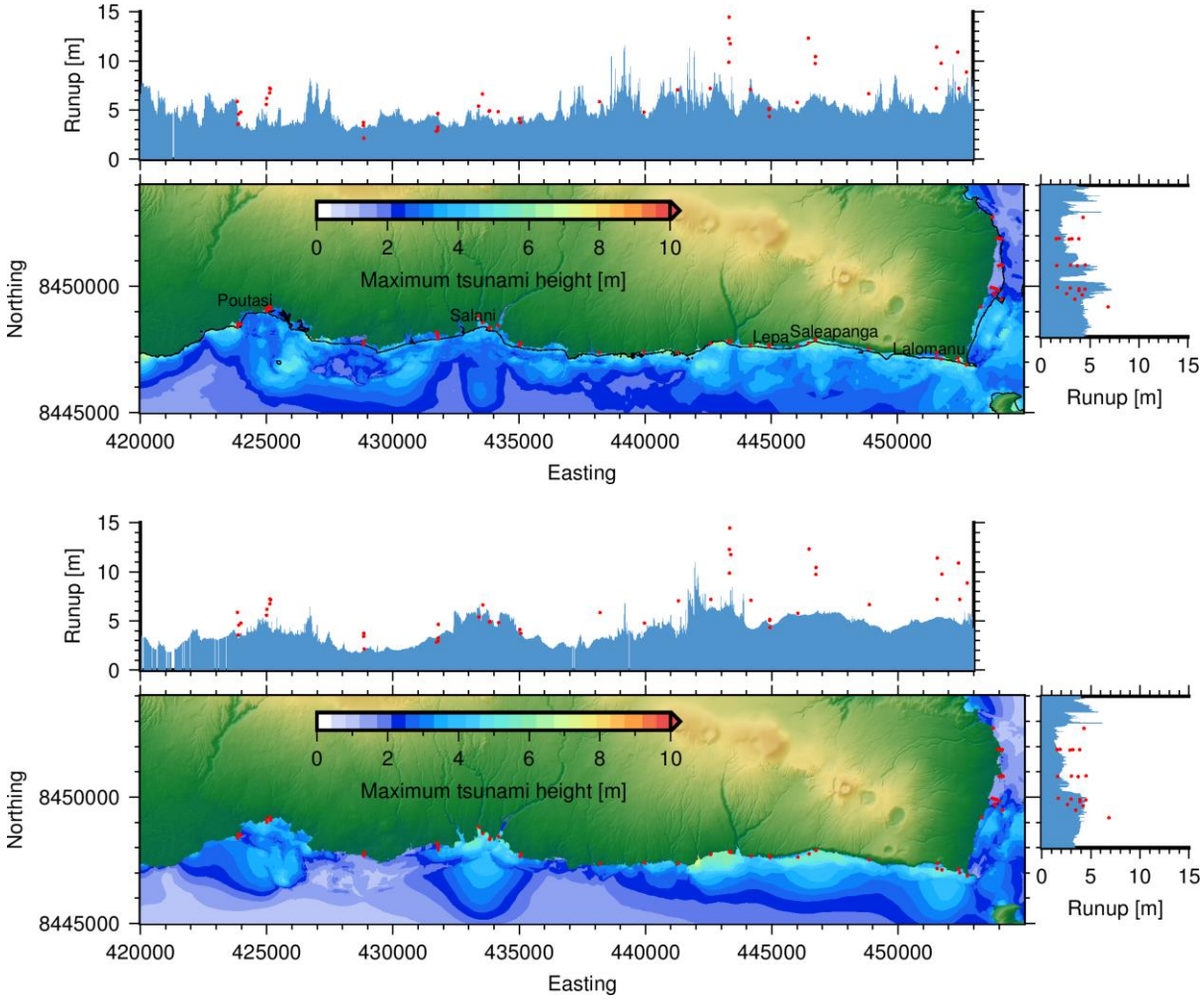

Figure 6. Comparison of computed with observed inundation on southeast Upolu using: (a) *Lay et al.* [2010] version C, and (b) *Hossen et al.* [2017].

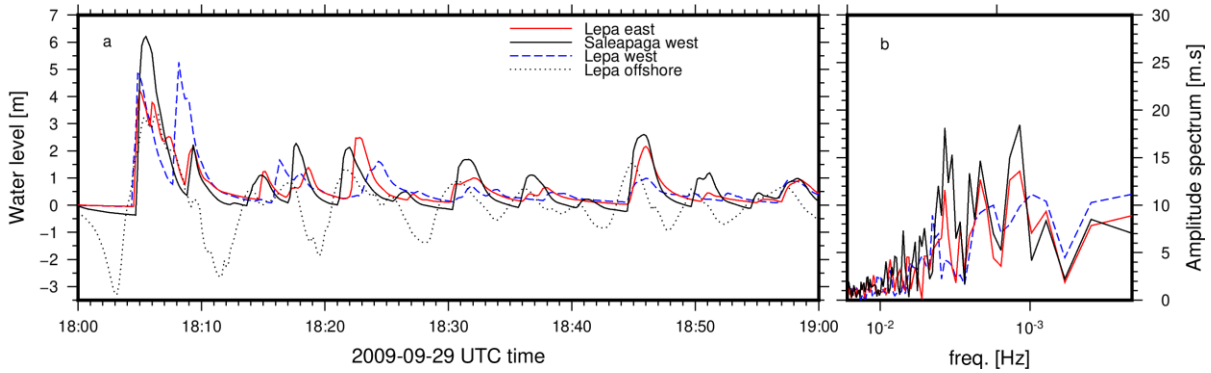

Figure 7. (a) Timeseries of water level for scenario *Lay et al.* [2010] version C showing the variability of onshore hydrodynamics response at Lepa and Saleapaga, and offshore of Lepa. (b) Amplitude spectrum showing local variability of onshore and offshore wave energy and excitation frequencies.

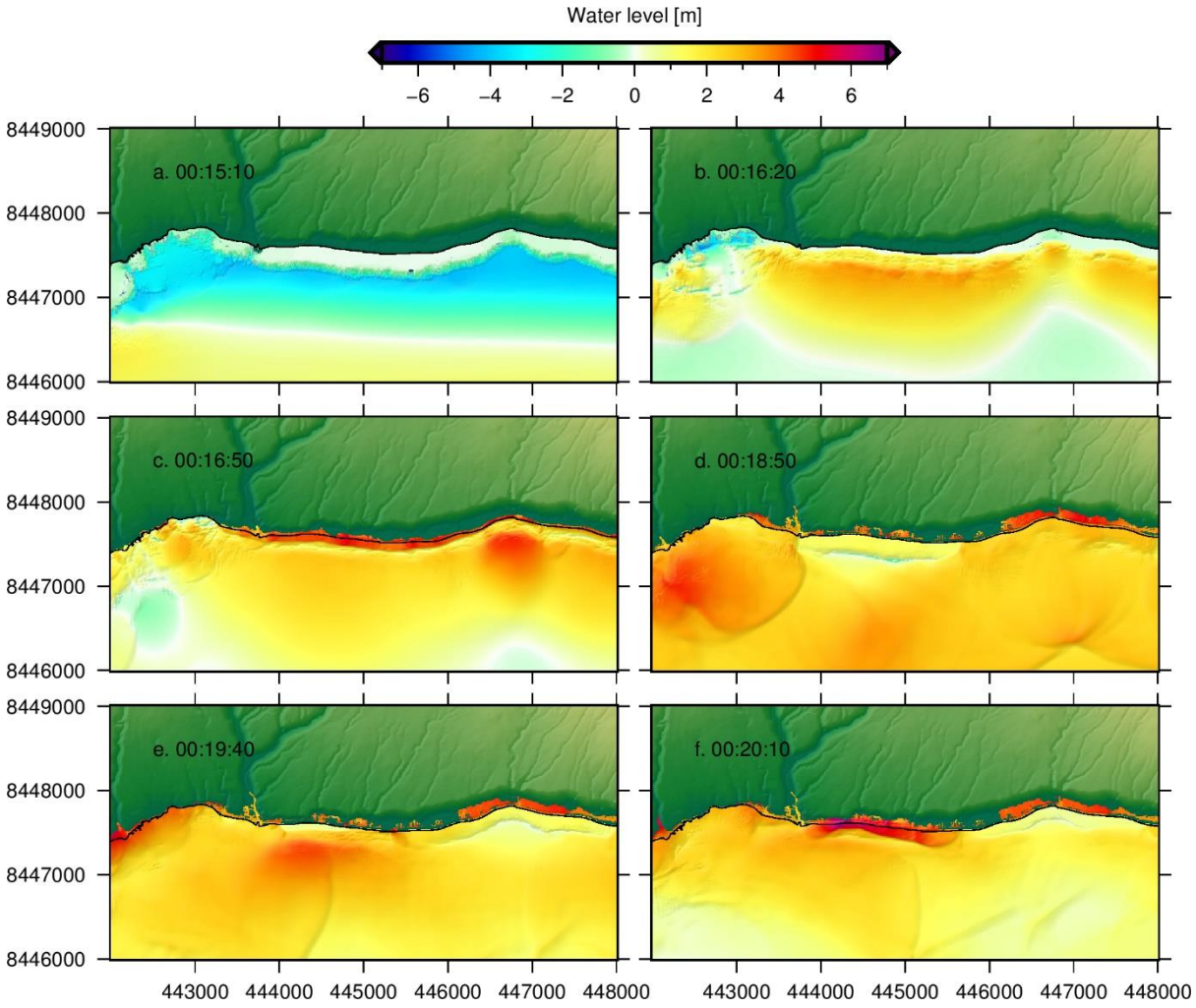

Figure 8. Sequence of inundation due to the first tsunami wave for scenario *Lay et al.* [2010] version C at Lepa and Saleapaga. The leading trough is represented by the initial draw-down of the first waves drying out the lagoon and reef foreshore, with the crest rising offshore. The model was calculated in UTM.

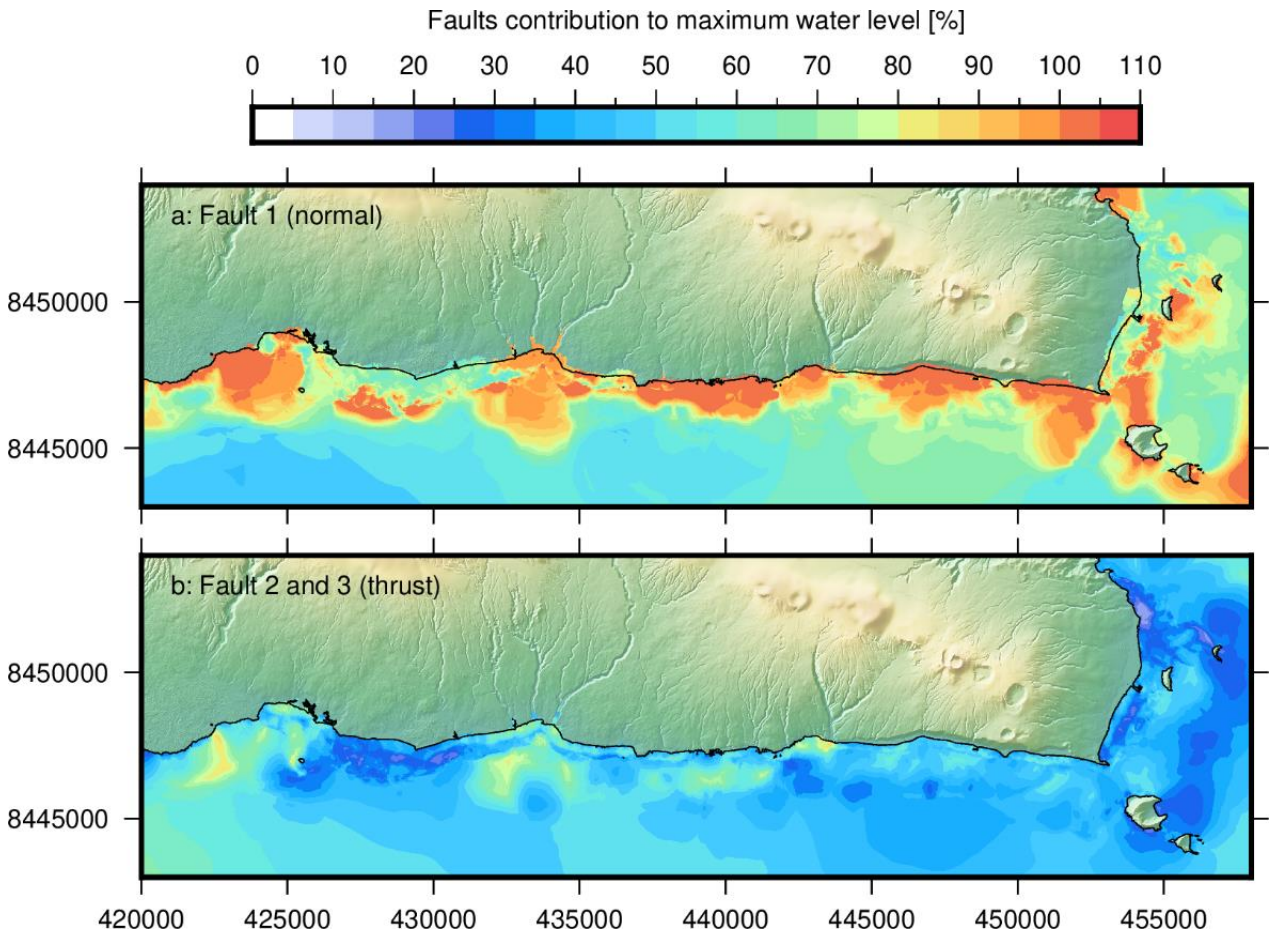

Figure 9. (a) Spatial distribution of Fault 1 (normal fault) contribution to maximum runup. (b) Spatial distribution of Faults 2 and 3 (reverse faults) contribution to maximum runup for scenario *Lay et al.* [2010] version C. Areas of orange/red are where the normal fault alone contributes to most/all of the inundation. Areas of blue/green are where thrust faults contributed 50/30 % of the runup. The model was calculated in UTM.

Journal of Geophysical Research: Oceans

Supporting Information for

Effects of source faulting and fringing reefs on the 2009 South Pacific tsunami inundation in southeast Upolu, Samoa

Cyprien Bosserelle[1], Shaun Williams[1], Kwok Fai Cheung[2], Thorne Lay[3], Yoshiki Yamazaki[2], Titimanu Simi[4†], Volker Roeber[5], Emily Lane[1], Ryan Paulik[1], Lameko Simanu[4]

[1]National Institute of Water and Atmospheric Research (NIWA), New Zealand. [2]Department of Ocean and Resources Engineering, University of Hawaii at Manoa, Hawaii, USA. [3]University of California Santa Cruz, California, USA. [4]Disaster Management Office, Ministry of Natural Resources and Environment, Apia, Samoa. [5]Université de Pau et des Pays de l'Adour (UPPA), HPC-Waves Laboratoire SIAME, Pau, France. [†]Current affiliation: Management Unit, Green Climate Fund, Samoa Ministry of Finance.

Contents of this file

Introduction

The supporting information includes Figures S1-S14 showing regional maximum water level, recorded and computed time series and spectra of surface elevations at DART water-level stations and the Apia tide gauge, measured and computed runup for the whole of Samoa and southeast Upolu, and computed vs observed inundation on southeast Upolu for each of the fourteen scenarios tested. Movie S1 provides an animation of the tsunami generation, propagation and inundation for our selected sources discussed in the main text.

Figure S1-S14. Regional maximum water level (top left); recorded (black) and computed (red) time series and spectra of surface elevations at DART water-level stations and the Apia tide gauge (right); measured and computed runup for the whole of Samoa (blue dots) and southeast Upolu (red dots) (middle left); computed vs observed inundation on southeast Upolu (bottom), for each of the 14 scenarios tested. These are consistent with the sources described in Table 1 of the main text.

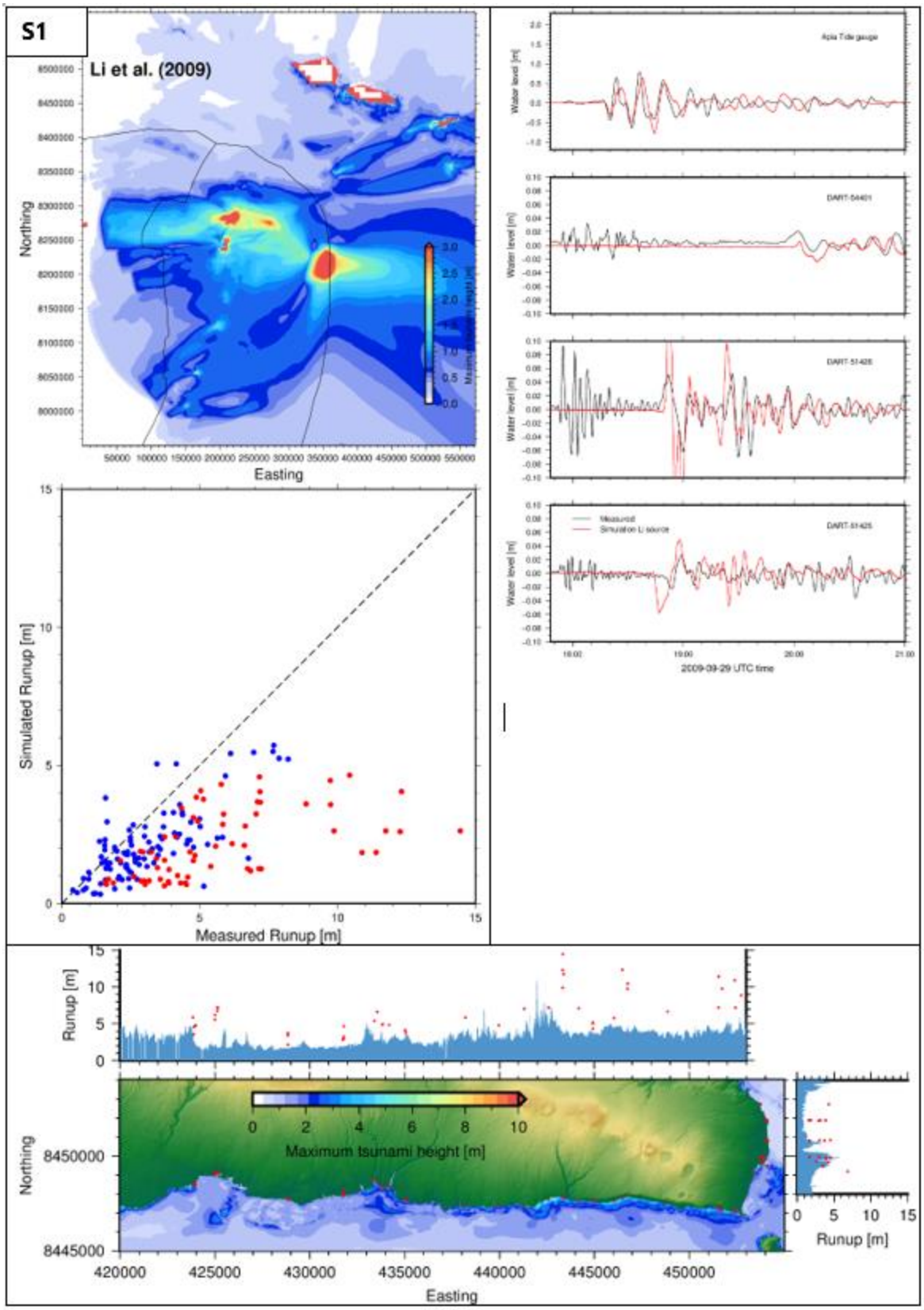
S1
Li et al. (2009)
Northing
Easting
Maximum tsunami height [m]
Simulated Runup [m]
Measured Runup [m]
Water level [m]
2009-09-29 UTC time
Measured
Simulation Li source
Runup [m]

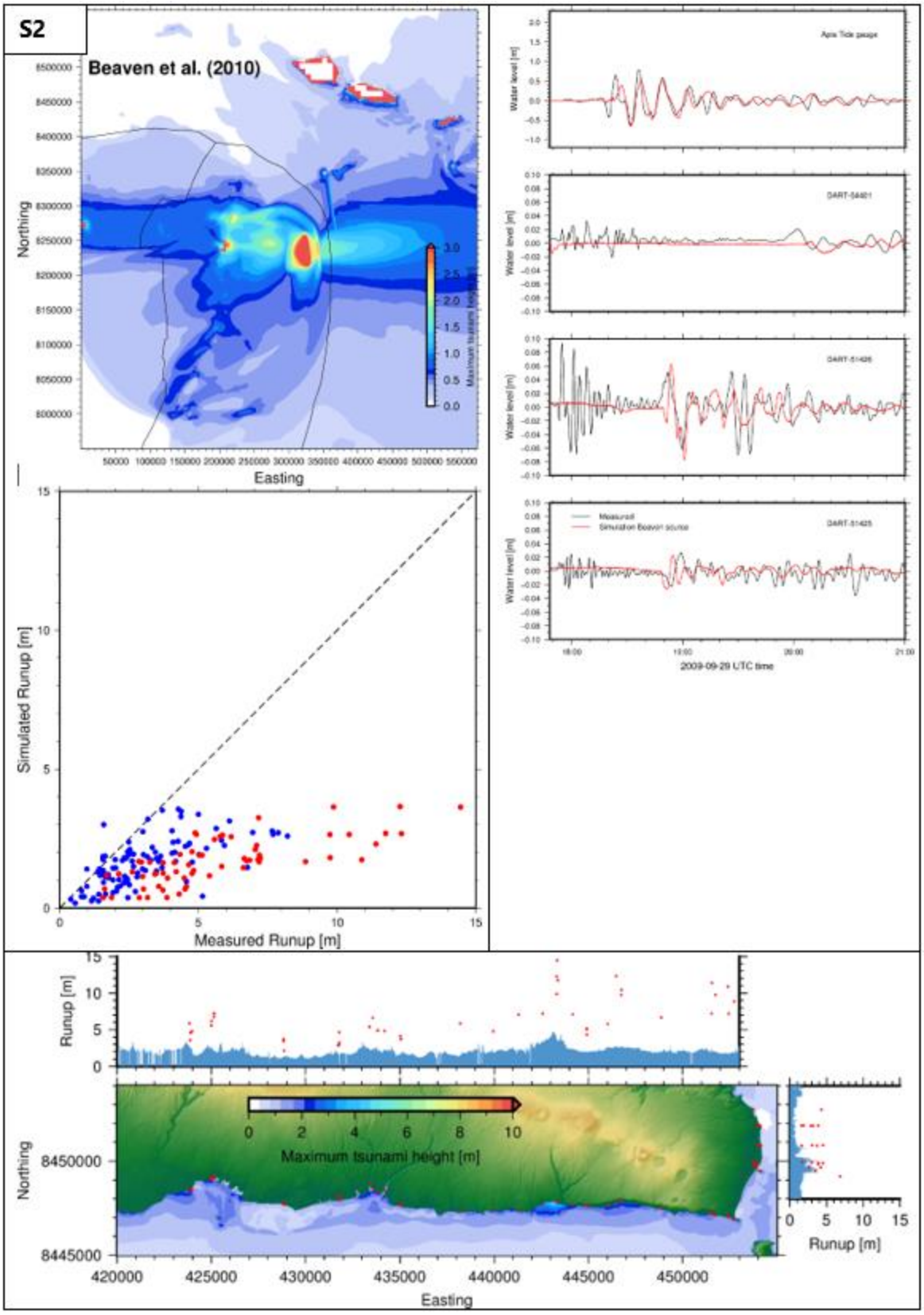
S2
Beaven et al. (2010)
Northing
Easting
Maximum tsunami height [m]
Apia Tide gauge
DART-54401
DART-51426
DART-51425
Water level [m]
Measured
Simulation Beaven source
2009-09-29 UTC time
Simulated Runup [m]
Measured Runup [m]
Runup [m]

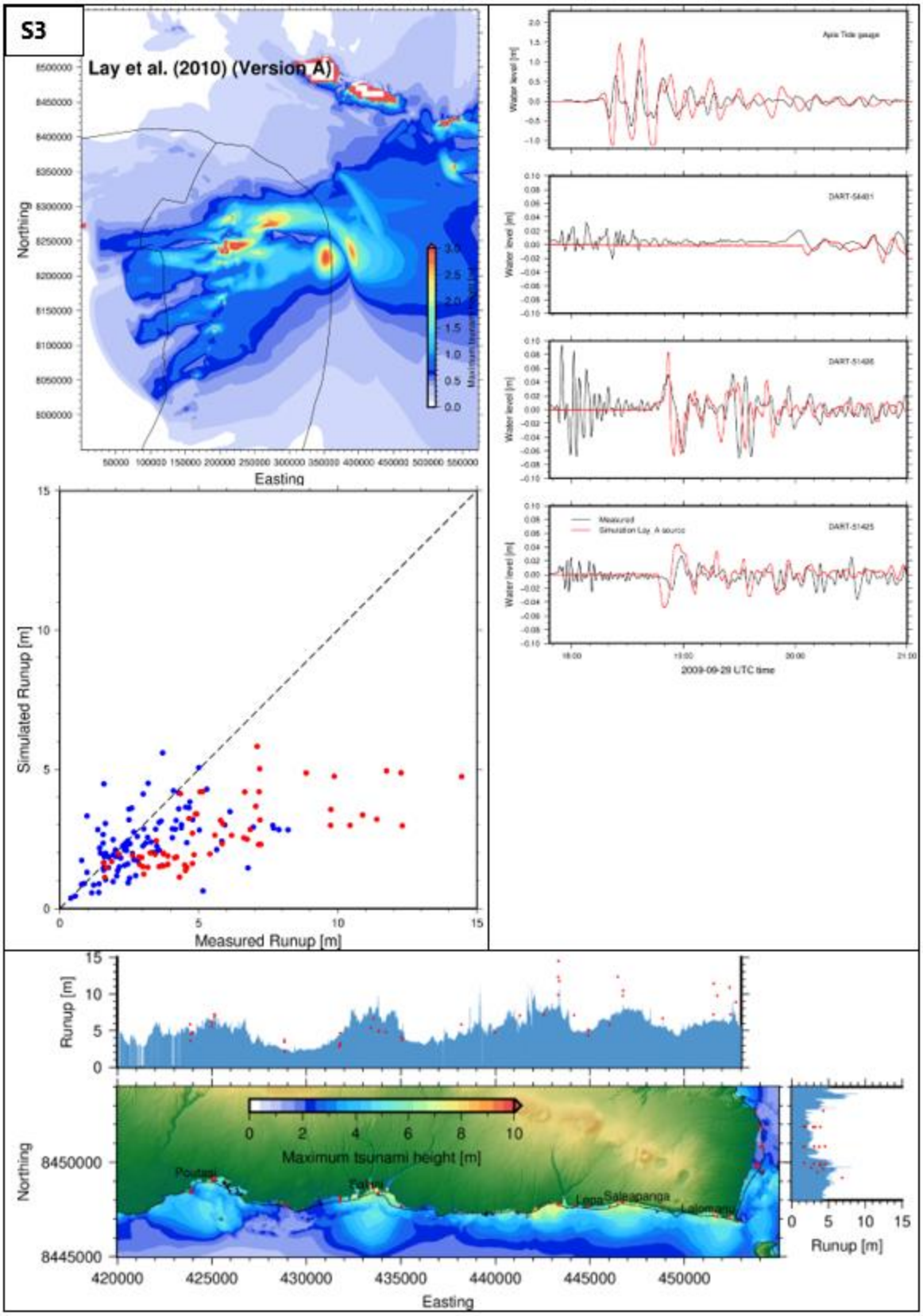
S3
Lay et al. (2010) (Version A)
Northing
Easting
Maximum tsunami height [m]
Apia Tide gauge
DART-54401
DART-51406
DART-51425
Water level [m]
Measured
Simulation Lay A source
2009-09-29 UTC time
Simulated Runup [m]
Measured Runup [m]
Runup [m]
Poutasi
Falelatai
Lepa
Saleapaga
Lalomanu

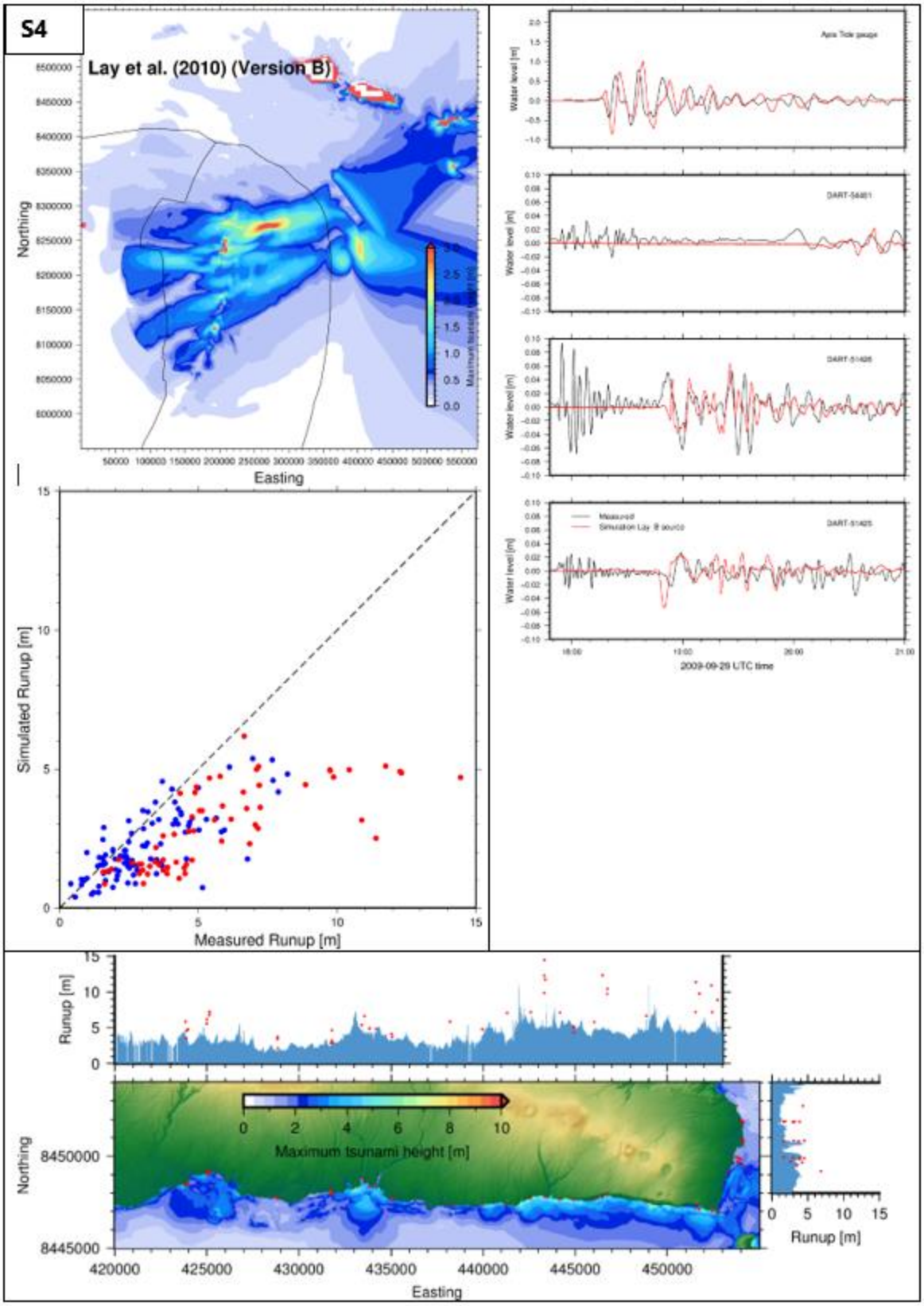
S4
Lay et al. (2010) (Version B)
Northing
Easting
Maximum tsunami height [m]
Apia Tide gauge
DART-54401
DART-51406
DART-51407
Measured
Simulation Lay B source
Water level [m]
2009-09-29 UTC time
Simulated Runup [m]
Measured Runup [m]
Runup [m]

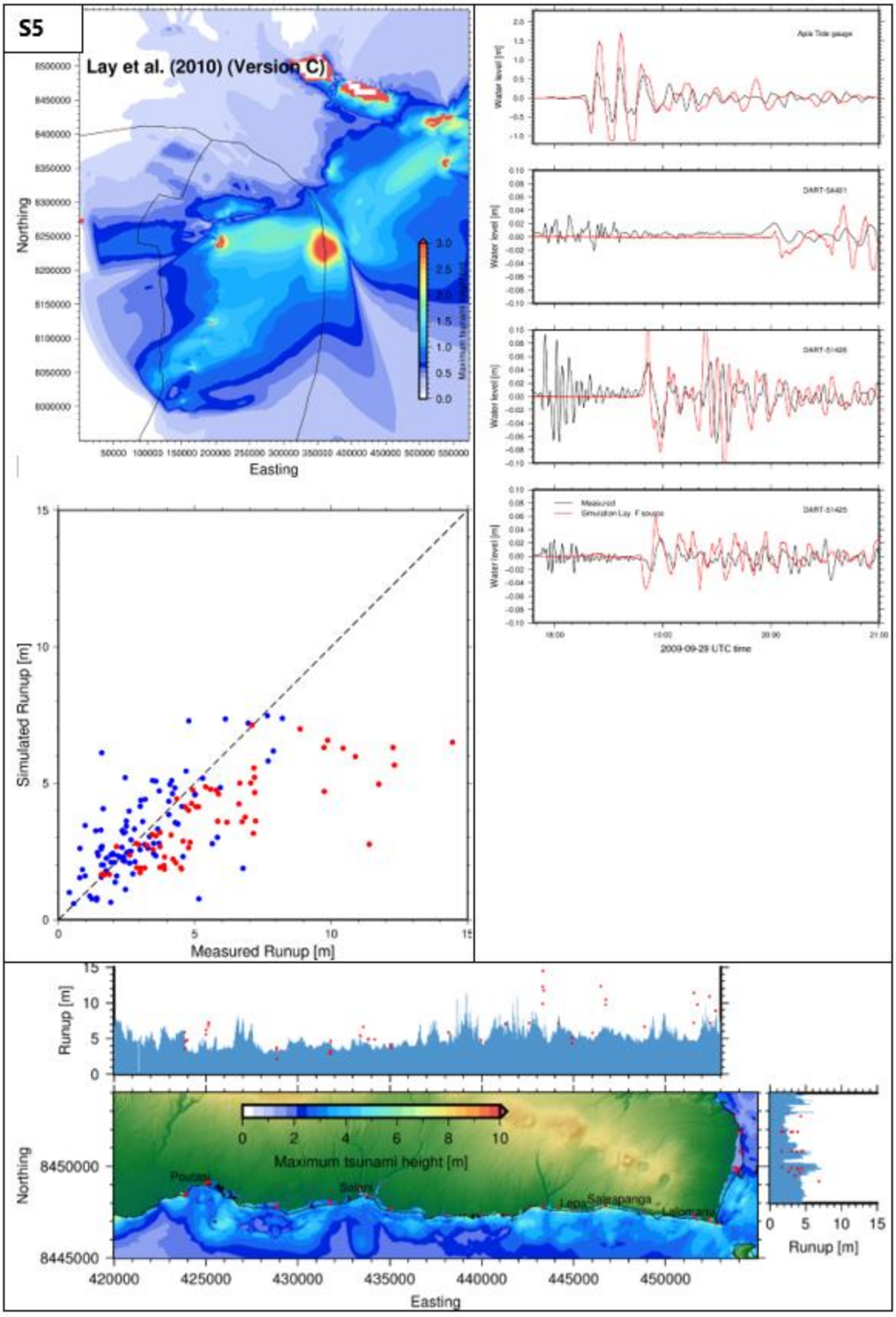
S5
Lay et al. (2010) (Version C)
Northing
Easting
Maximum tsunami height [m]
Apia Tide gauge
DART-54401
DART-51406
DART-51425
Water level [m]
Measured
Simulation Lay F sources
2009-09-29 UTC time
Simulated Runup [m]
Measured Runup [m]
Runup [m]
Pouiai
Salvo
Lepa
Saleapaga
Leloaloa

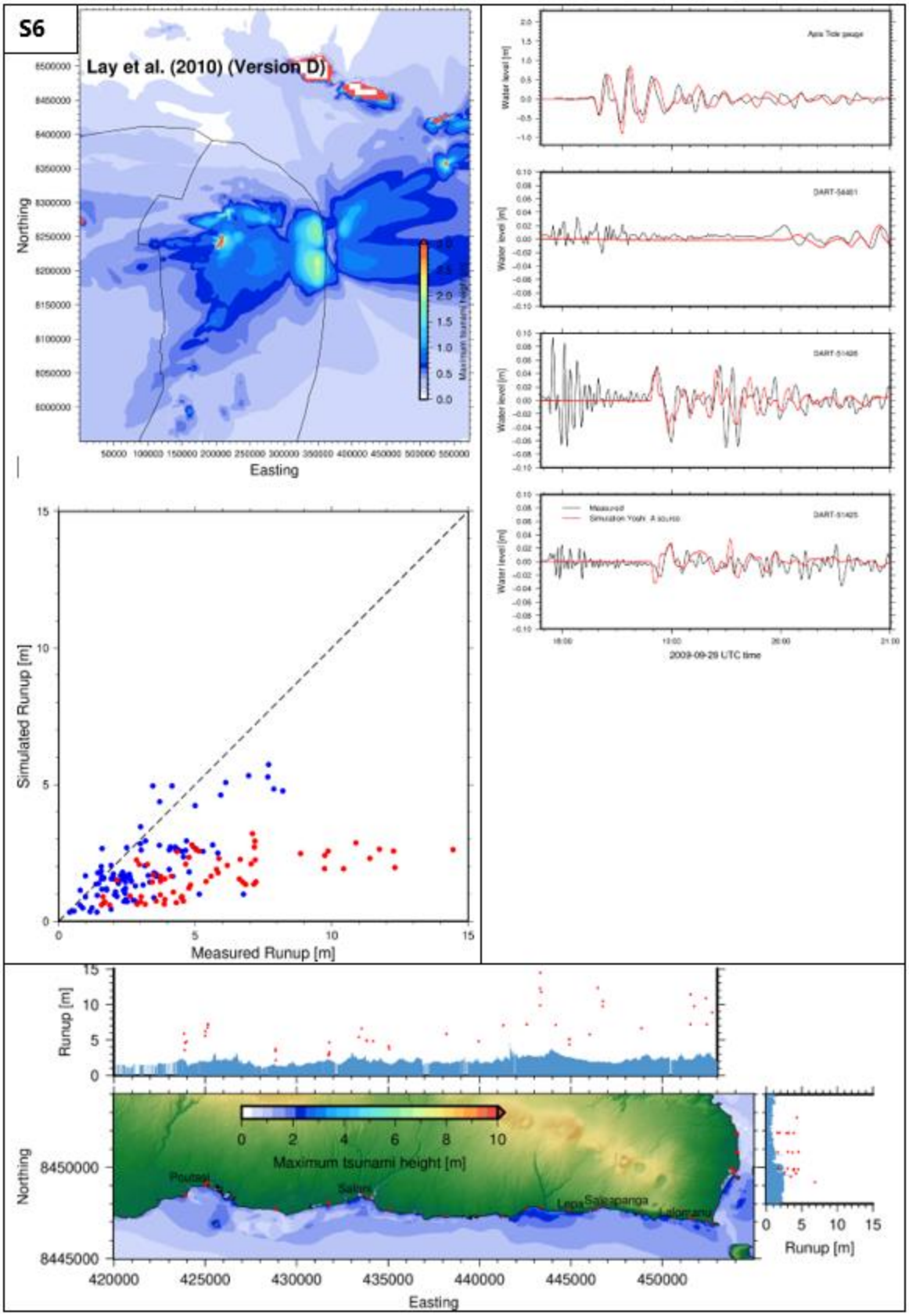
S6
Lay et al. (2010) (Version D)
Northing
Easting
Maximum tsunami height [m]
Water level [m]
2009-09-29 UTC time
Simulated Runup [m]
Measured Runup [m]
Runup [m]
Maximum tsunami height [m]
Poutasi
Satitoa
Lepa
Salapanga
Lalomanu
Northing
Easting

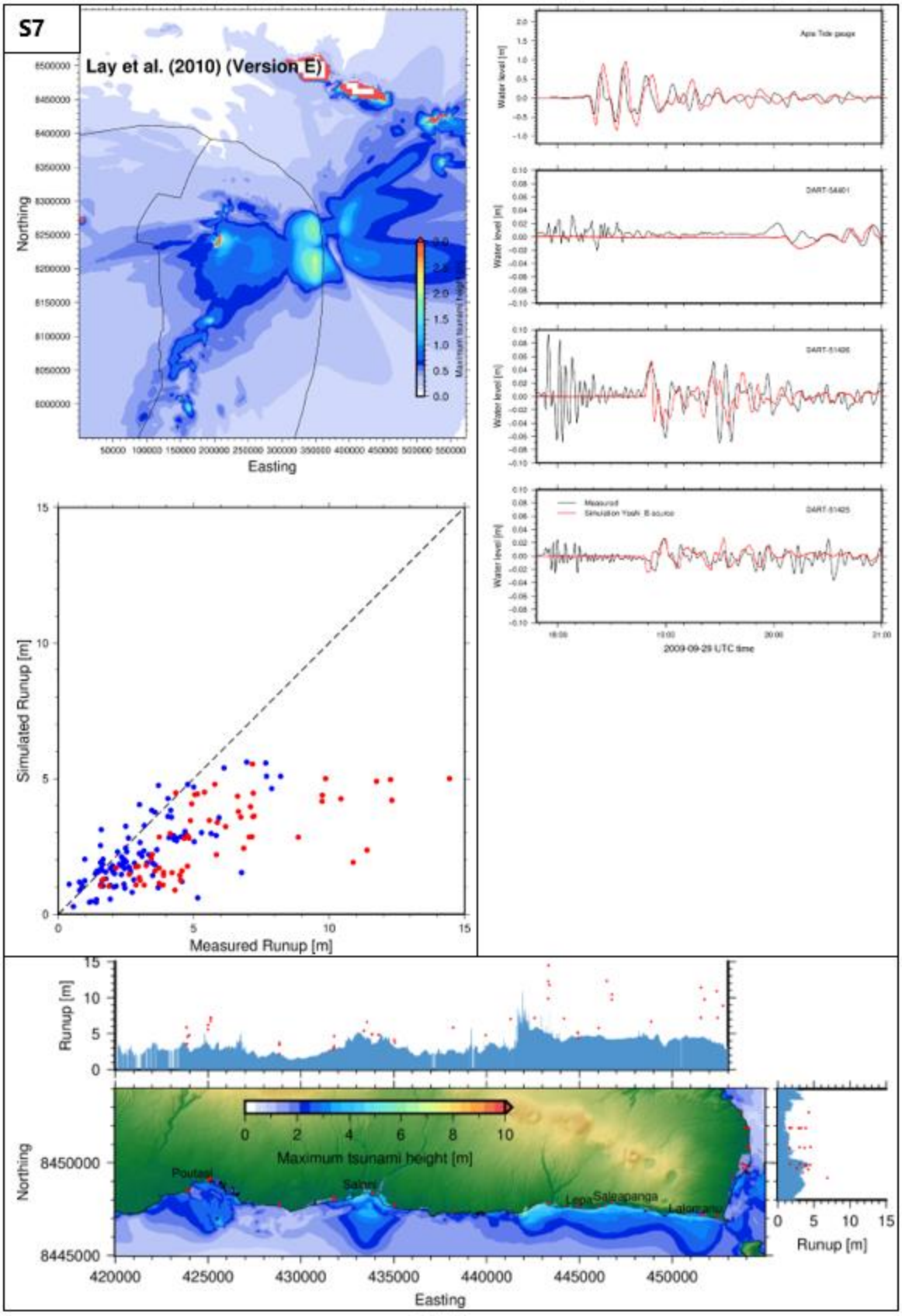
S7
Lay et al. (2010) (Version E)
Northing
Easting
Maximum tsunami height [m]
Water level [m]
2009-09-29 UTC time
Measured
Simulation from E source
Simulated Runup [m]
Measured Runup [m]
Runup [m]
Maximum tsunami height [m]
Poutasi
Satapo
Lepa
Saleapaga
Lalomanu

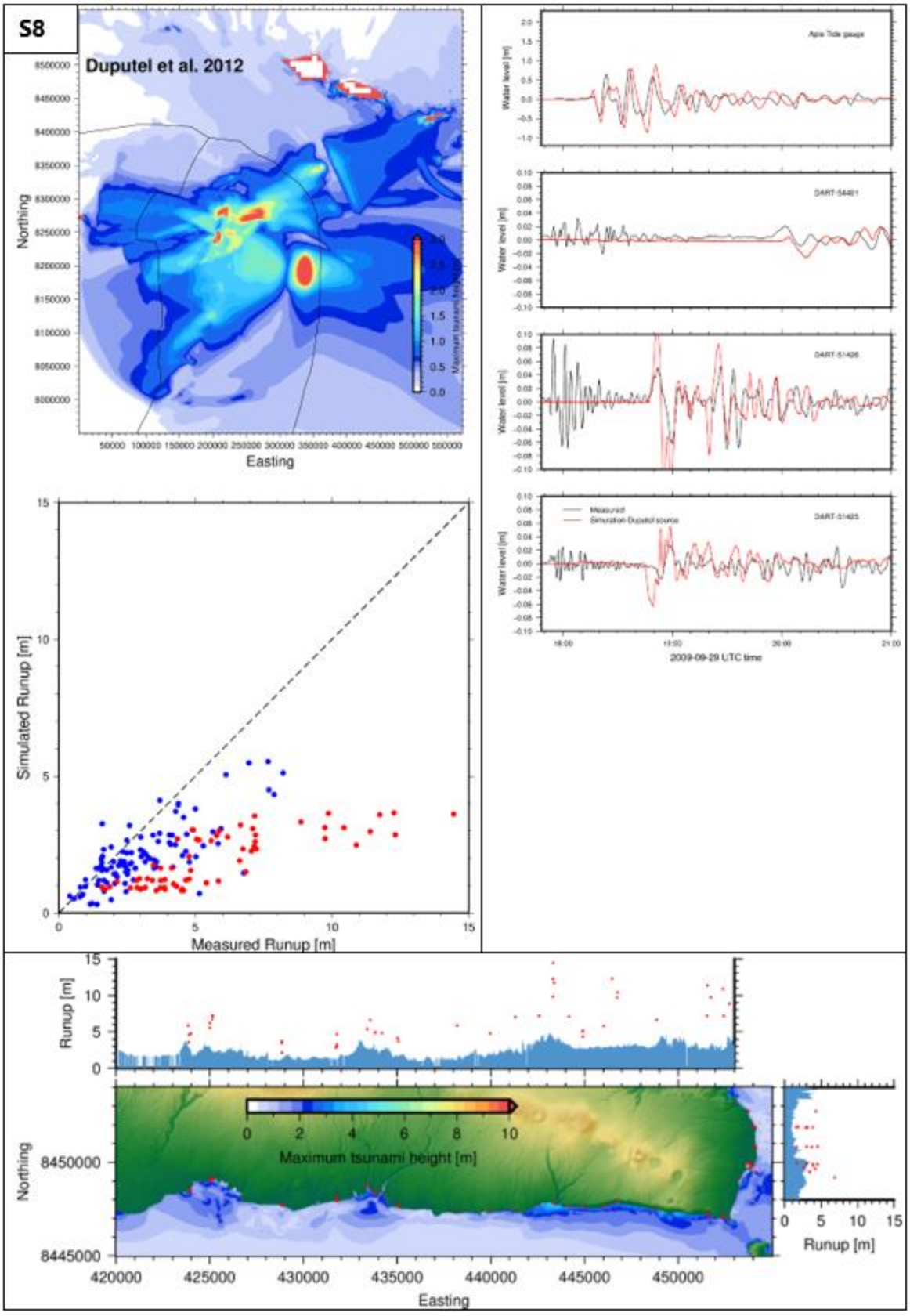
S8
Duputel et al. 2012
Northing
Easting
Water level [m]
2009-09-29 UTC time
Simulated Runup [m]
Measured Runup [m]
Runup [m]
Maximum tsunami height [m]

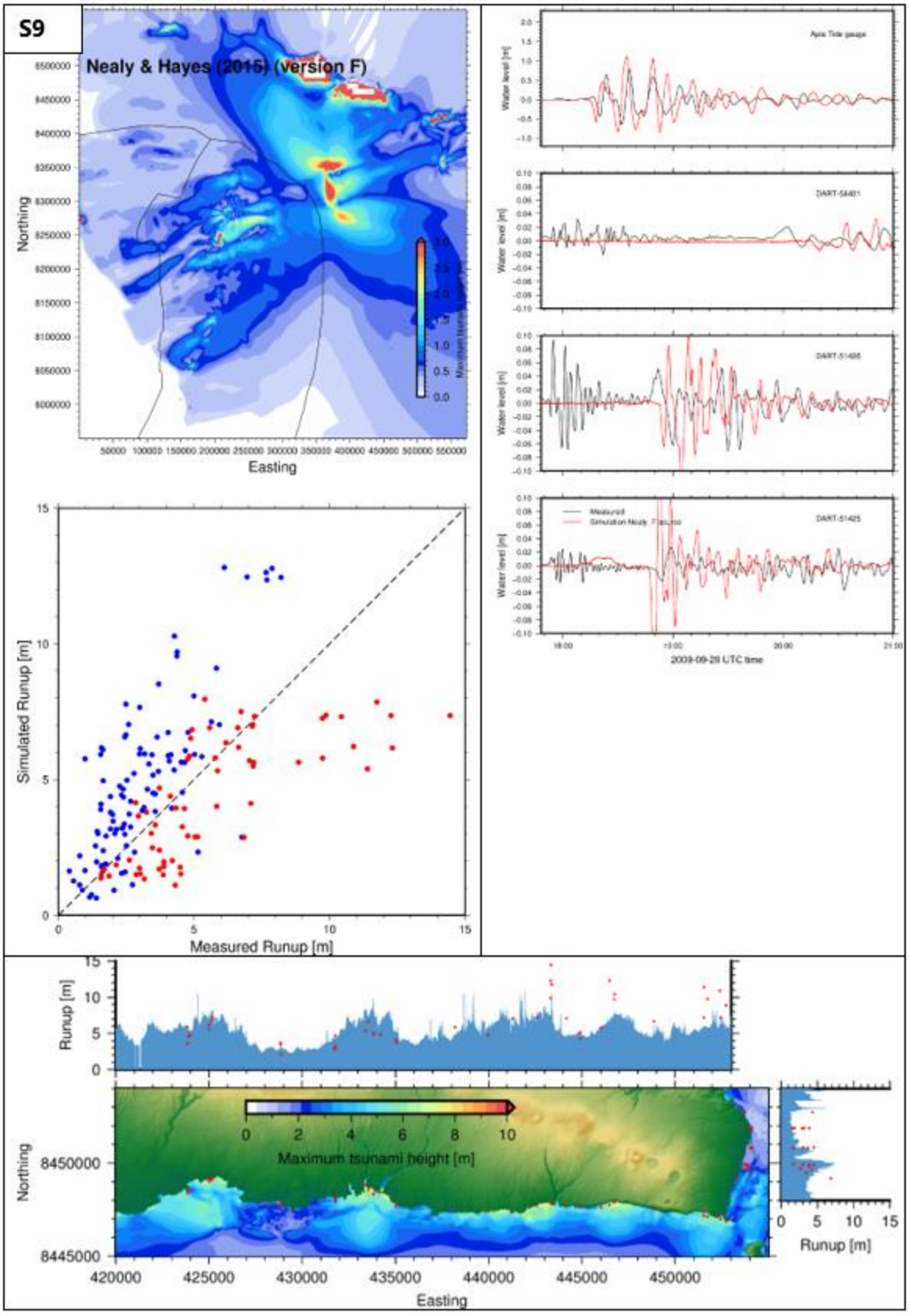
S9
Nealy & Hayes (2015) (version F)
Northing
Easting
Apia Tide gauge
DART-54401
DART-51406
DART-51425
Water level [m]
Measured
Simulation Nealy Fault no
2009-09-29 UTC time
Simulated Runup [m]
Measured Runup [m]
Runup [m]
Maximum tsunami height [m]
Northing
Easting
Runup [m]

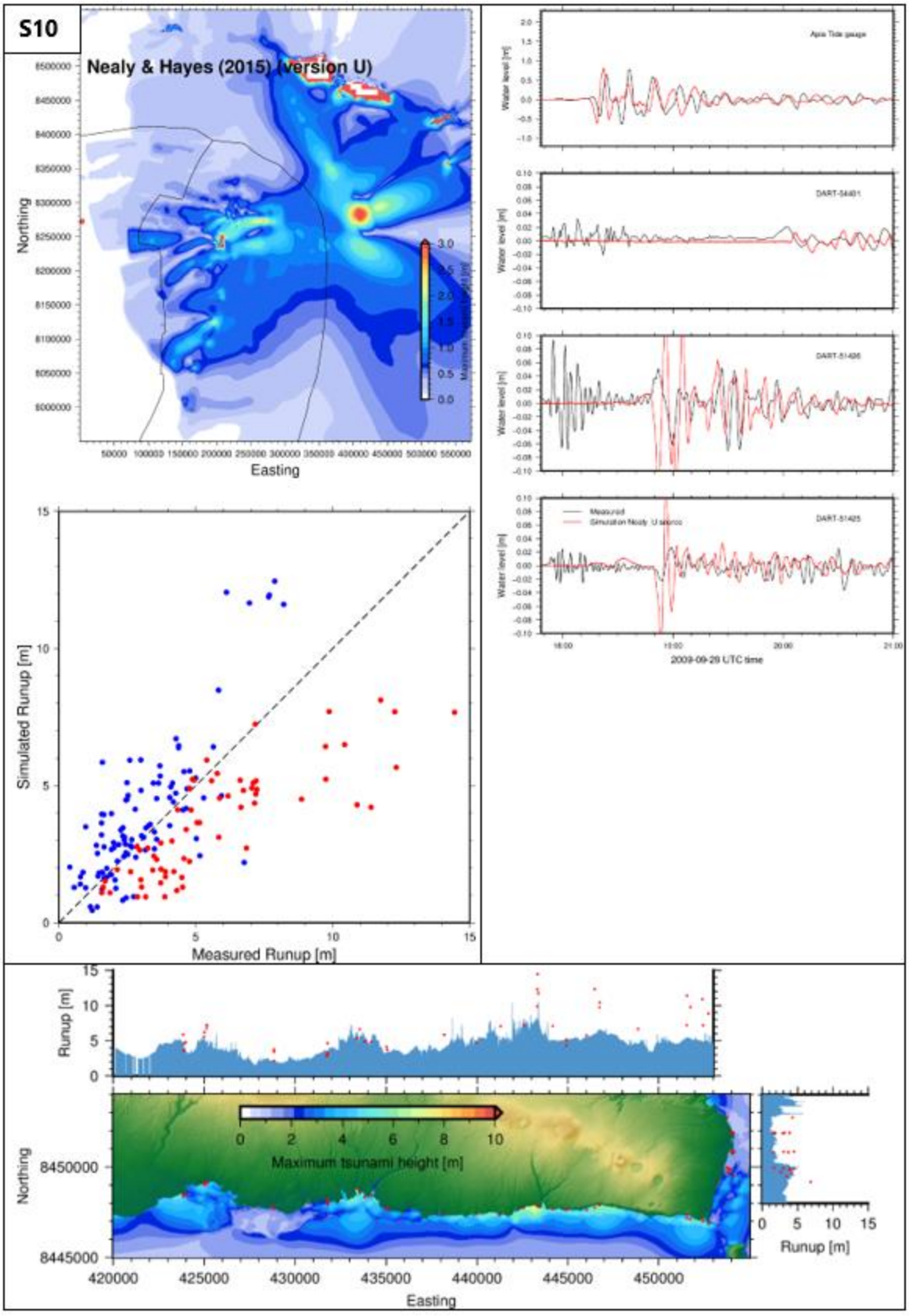
S10
Nealy & Hayes (2015) (version U)
Northing
Easting
Water level [m]
2009-09-29 UTC time
Simulated Runup [m]
Measured Runup [m]
Runup [m]
Maximum tsunami height [m]

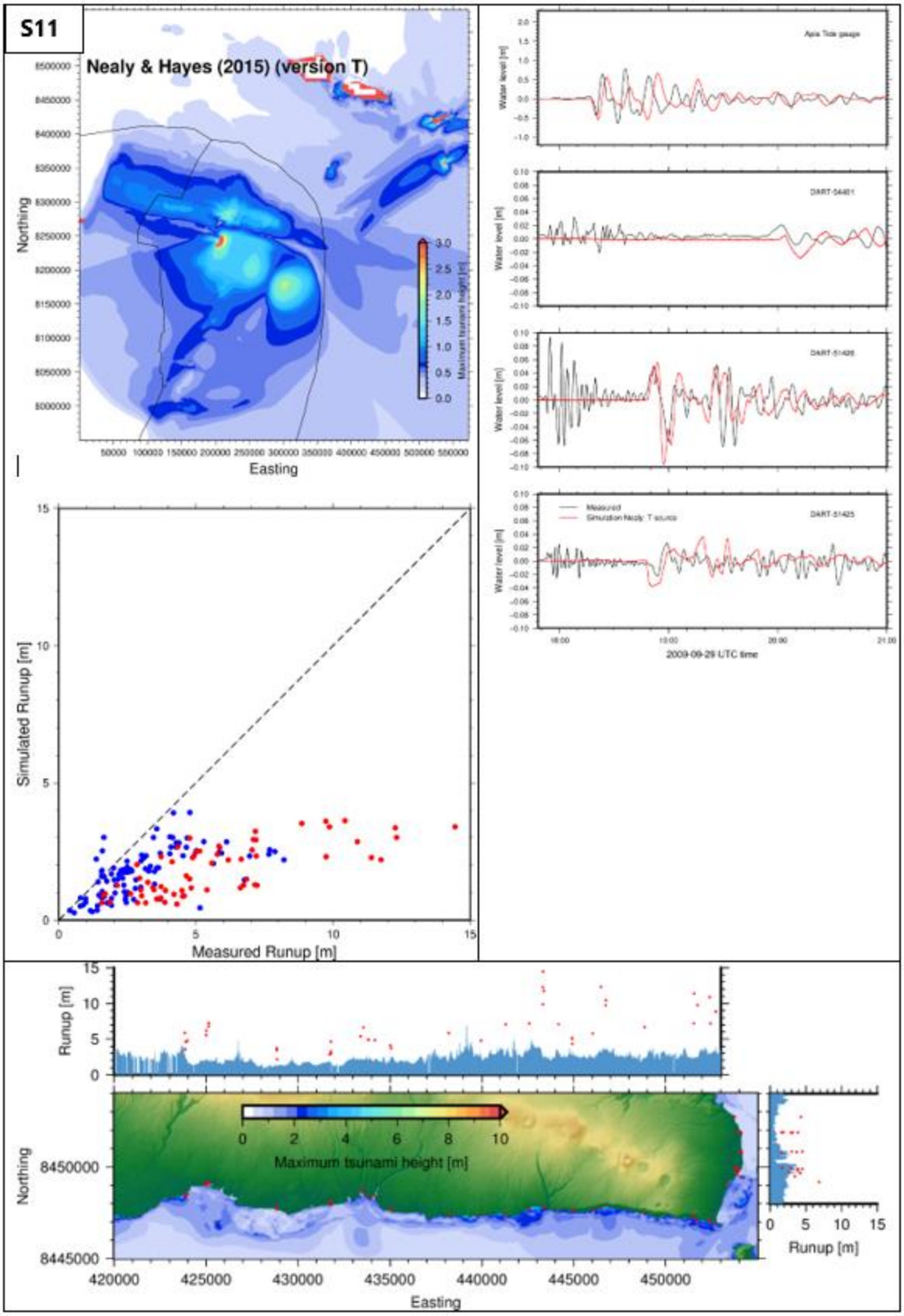
S11
Nealy & Hayes (2015) (version T)
Northing
Easting
Maximum tsunami height [m]
Apia Tide gauge
DART-54401
DART-51426
DART-51425
Water level [m]
Measured
Simulation Nealy T source
2009-09-29 UTC time
Simulated Runup [m]
Measured Runup [m]
Runup [m]
Maximum tsunami height [m]
Northing
Easting

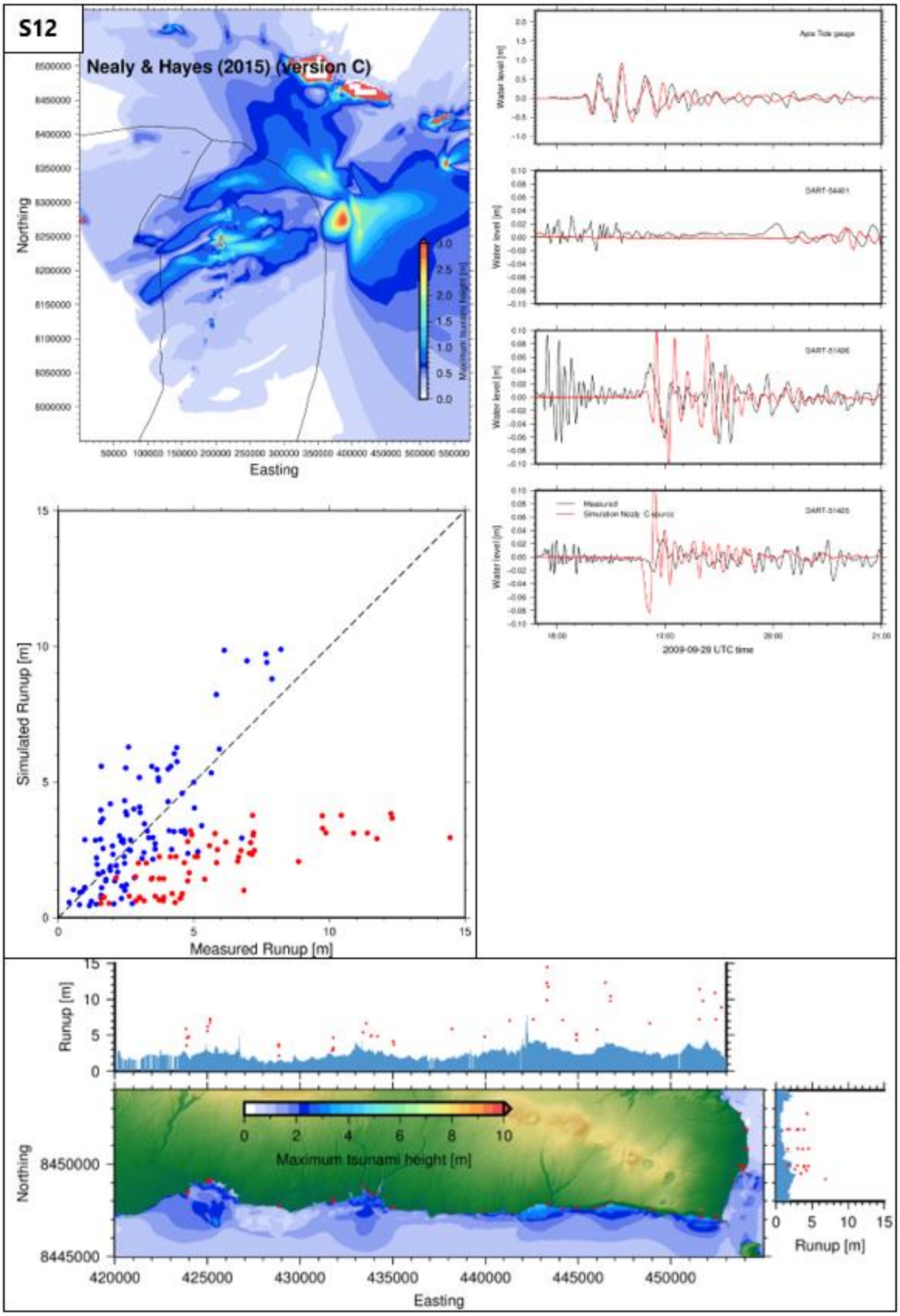
S12
Nealy & Hayes (2015) (version C)
Northing
Easting
Maximum tsunami height [m]
Apia Tide gauge
DART-54401
DART-51406
DART-51425
Water level [m]
Measured
Simulation Nealy C source
2009-09-29 UTC time
Simulated Runup [m]
Measured Runup [m]
Runup [m]
Northing
Easting
Maximum tsunami height [m]
Runup [m]

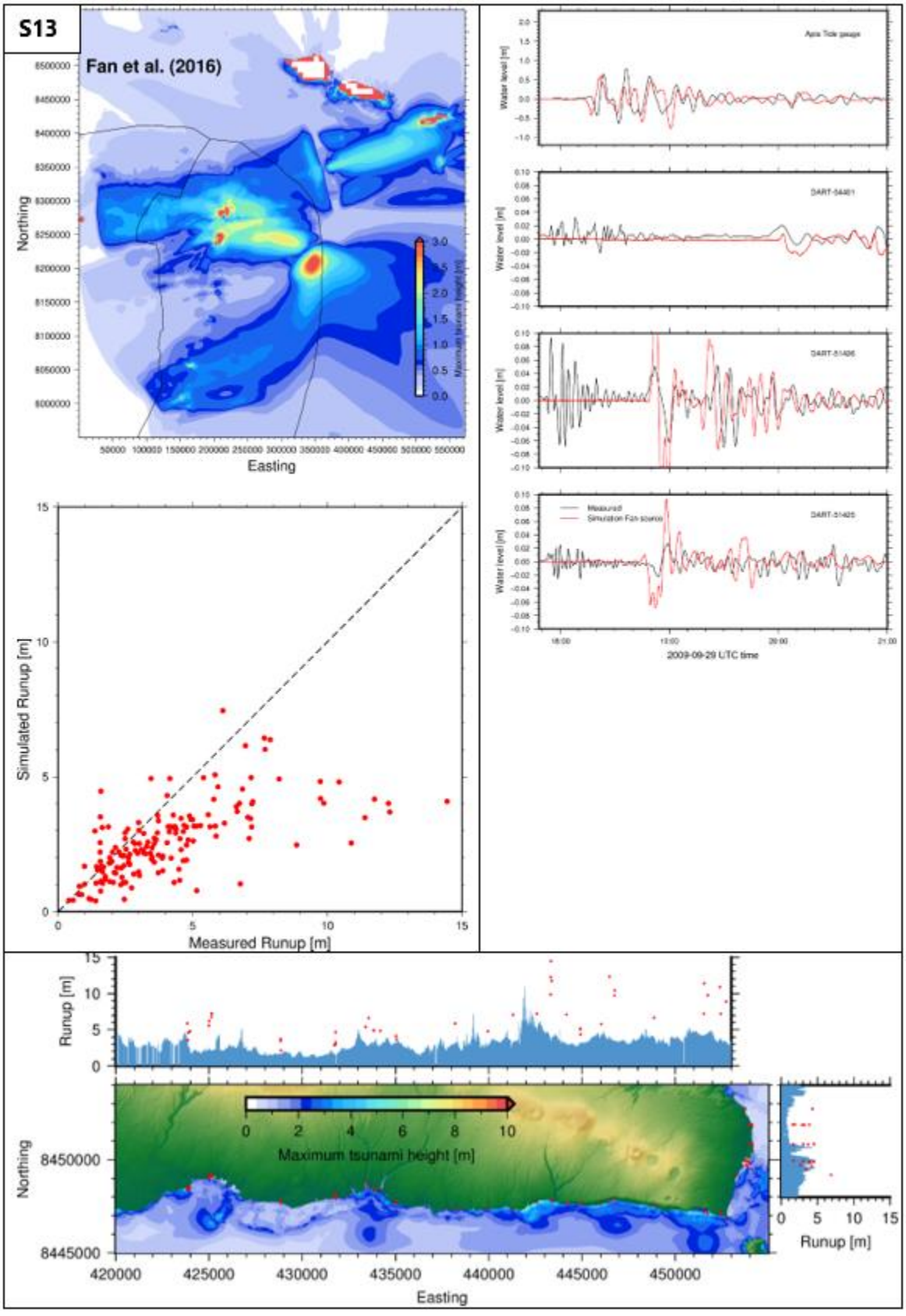
S13
Fan et al. (2016)
Northing
Easting
Apia Tide gauge
DART-54401
DART-51406
DART-51425
Measured
Simulation Fan source
Water level [m]
2009-09-29 UTC time
Simulated Runup [m]
Measured Runup [m]
Runup [m]
Maximum tsunami height [m]

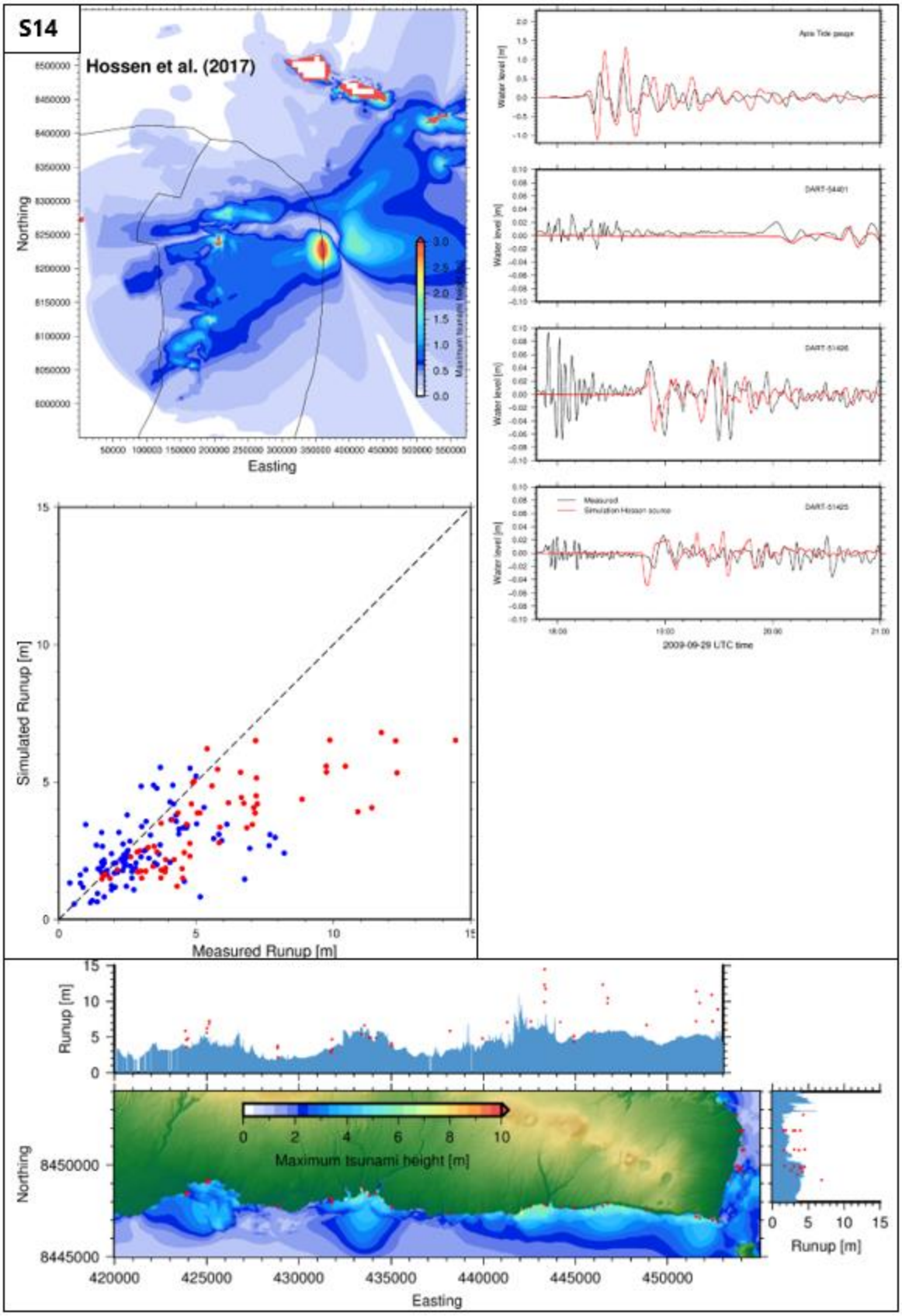
S14
Hossen et al. (2017)
Northing
Easting
Maximum tsunami height [m]
Apra Tide gauge
DART-54401
DART-51406
DART-51425
Measured
Simulation Hossen source
Water level [m]
2009-09-29 UTC time
Simulated Runup [m]
Measured Runup [m]
Runup [m]
Maximum tsunami height [m]

Movie S15. Animation of the 2009 tsunami from initiation to inundation in Samoa; (available for download at https://doi.org/10.5281/zenodo.4054271).